Magnetometry of low-dimensional electron and hole systems

TOPICAL REVIEW

Magnetometry of low-dimensional electron and hole systems

A Usher[1] and M Elliott[2]

[1] School of Physics, University of Exeter, Stocker Road, Exeter EX4 4QL, UK
[2] School of Physics and Astronomy, Cardiff University, Queens Buildings, Cardiff CF24 3AA, UK

E-mail: a.usher@exeter.ac.uk and elliottm@cf.ac.uk

Abstract
The high-magnetic-field, low-temperature magnetic properties of low-dimensional electron and hole systems reveal a wealth of fundamental information. Quantum oscillations of the thermodynamic equilibrium magnetization yield the total density of states, a central quantity in understanding the quantum Hall effect in 2D systems. The magnetization arising from non-equilibrium circulating currents reveals details, not accessible with traditional measurements, of the vanishingly small longitudinal resistance in the quantum Hall regime. We review how the technique of magnetometry has been applied to these systems, the most important discoveries that have been made, and their theoretical significance.

(Some figures in this article are in colour only in the electronic version)

Contents

Introduction

In this review we outline how magnetometry measurements have been used to examine the electronic properties of low-dimensional systems, primarily the quasi-two-dimensional electron system (2DES) formed in gallium–arsenide-based heterostructures. We have divided the review into three sections: in section 2 we consider the oscillatory magnetic moment, i.e. the de Haas–van Alphen (dHvA) effect, observed in a 2DES in *thermodynamic equilibrium* at low temperatures and high magnetic fields. This essentially quantum mechanical effect, originally discovered almost eighty years ago in bismuth, has proved extraordinarily powerful in probing electronic properties around the Fermi energy. In section 3 we examine *non-equilibrium* magnetic moments arising from circulating induced currents. These currents, detected at particular magnetic field ranges in the regime of the quantum Hall effect (QHE), provide complementary information to traditional electrical transport measurements. They have far greater sensitivity to the resistance minima of the quantum Hall state, and reveal quite unexpected results in the breakdown of the QHE at high-current densities. To begin with however, in section 1 we examine how these experimental studies on

low-dimensional systems have been enabled by the development of highly sensitive magnetometers over the past twenty-five years or so. Readers who are interested only in the scientific outcome of the experiments, rather than in the techniques themselves, can skip this material and go straight to section 2.

1. Magnetometry development

Measurements of the thermodynamic quantities such as magnetization or heat capacity in a 2DES represent a considerable experimental challenge because the size of the signal is proportional to the number of electrons in the sample. For a typical magnetization (dHvA) measurement of a 3D metal (of volume 1 mm^3), there are 10^{20} electrons; in a typical measurement of a 2DES (area 10 by 10 mm and having 10^{16} electrons m^{-2}) there are 10^{12}. As we shall see in section 2.1 the theoretical amplitude of the dHvA oscillations in the latter case (two effective Bohr magnetons per electron) would be 2.8×10^{-10} J T^{-1}. In addition to the challenges of tiny signal sizes, the measurements need to be made in high magnetic fields (up to around 20 T) and at low temperatures (from a few kelvin down to millikelvin).

The first attempt to measure the dHvA effect in a 2DES used a commercial superconducting quantum interference device (SQUID) magnetometer [1]. Although the sensitivity of a SQUID is quantum-limited when operated in low magnetic fields, its performance is severely degraded in high magnetic fields. In this experiment the magnetic moment sensitivity was 10^{-10} J T^{-1} with an averaging time per data point of 30 min. It required a 2DES of overall area 240 cm^2 consisting of ~23 pieces of a multiple-quantum-well structure containing 173 wells, stacked together to form a total of ~ 4000 2DES layers. The measurement was restricted to magnetic fields less than 5 T and yielded dHvA oscillations 30 times smaller than expected (probably because of inter-layer inhomogeneity). The observation of $1/B$ periodic dHvA oscillations was nevertheless a remarkable achievement at the time. The only other SQUID magnetometry study of 2DES [2] demonstrated a much improved sensitivity of 7×10^{-14} J T^{-1} at a maximum field of 10 T, using a thin-film dc SQUID with integrated multi-turn input coil and incorporating NbN–MgO–NbN Josephson junctions. A first-order gradiometer was attached to the input coil to form a flux transformer and the 2DES was placed within one of the gradiometer pick-up loops. The SQUID itself was placed in a remote, magnetically shielded location within the cryostat. A gate was used to modulate the 2DES number density at a frequency of 1.2 kHz, at which the SQUID noise was lowest. The sensitivity of this instrument enabled signals to be detected from both odd-integer and fractional QHEs [3]. However the method did have one distinct disadvantage, that the modulation of the 2DES number density makes the measurement highly perturbative, and is likely to result in large induced currents [4], of which the authors were unaware at the time.

A useful figure-of-merit in comparing magnetometers is the resolution R in effective Bohr magnetons (defined in section 2.1.4) per electron. This resolution takes into account the size of the 2DES, as well as the magnetic moment sensitivity of the magnetometer. In specifying this for the different instruments reviewed here, we will assume a single-layer 2DES of number density 10^{16} m^{-2} having the maximum area that the instrument can accommodate (without stacking), and use magnetic moment resolutions determined at 5 T. We shall assume a measurement bandwidth of 1 Hz. It is important to note that these conditions may not coincide with those chosen by other authors in specifying their magnetometers' performance, but are chosen to provide consistency in comparisons made within this review. Using this definition, the resolution of the first SQUID instrument is 504 μ_B^*/e and for the later SQUID instrument it is 0.004 μ_B^*/e.

Nearly all other 2DES magnetization measurements have used torque magnetometers. (It is interesting that the discovery of the dHvA effect [5] was also made using a torque magnetometer.) These use a spring to convert the torque $\boldsymbol{m} \times \boldsymbol{B}$, produced by the 2DES magnetic moment $\boldsymbol{m}$ in the applied magnetic field $\boldsymbol{B}$, into a displacement of the sample. The displacement can then be detected using capacitive, optical-lever or piezo-electric techniques. The spring constant K determines the sensitivity of the device. Typically the resolution of such a device when placed in a high magnetic field, low-temperature environment is limited by vibrations of the cryostat which couple to the movement of the sample. In this limit, further reduction in K does not improve resolution; instead one has either to reduce vibrations at source, or to opt for a magnetometer design which is relatively insensitive to vibrations. Torque magnetometers subjected to uniform magnetic fields are sensitive to sources of anisotropic magnetization, such as 2DES, and do not detect isotropic magnetization. However, if a magnetic field gradient is also present, they do become sensitive to the isotropic component as well.

Torque magnetometers divide into two categories: torsion-balance magnetometers and cantilever magnetometers. Cantilever devices have the advantage that their deflection is governed by the Young modulus of the spring, which is typically ten times smaller than the torsional modulus which determines the deflection of torsion-balance instruments. However, the torsion-balance design is able to support larger and heavier samples.

1.1. Torsion-balance magnetometers

The first torque magnetometry studies of 2DES used the instrument shown schematically in figure 1(a) [6–9]. The torsion fibre was a wire, 37 μm diameter, 2 cm long, made from Pt–W alloy, which was suspended between two plastic supports. A plastic disc was mounted on the fibre with its face perpendicular to the fibre. On one side of the disc a semicircular capacitance electrode was evaporated, and electrically connected to the wire. The sample was also attached to this disk assembly, with the normal to the 2DES plane tilted at a small angle with respect to the applied magnetic field. Two fixed pie-shaped electrodes were placed parallel to and about 150 μm from the semicircular one, without touching the fibre, forming a differential capacitor.
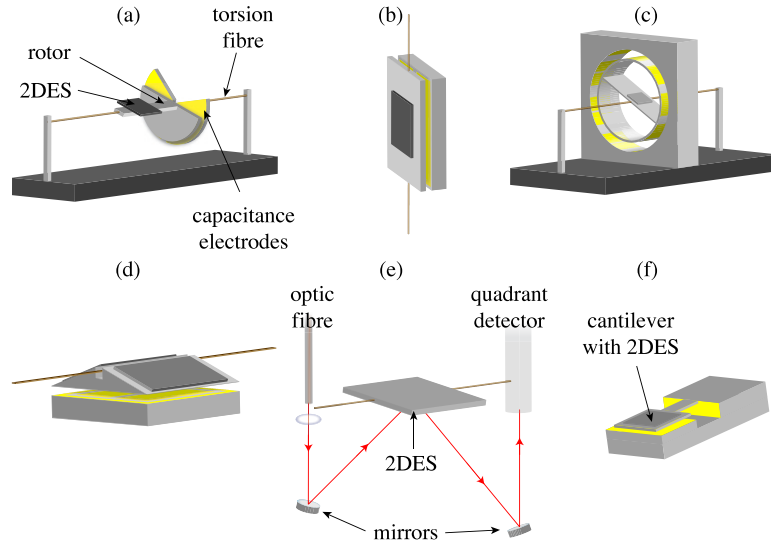
Figure 1. Schematic diagrams of the magnetometers of: (a) Eisenstein *et al* [6]; (b) Templeton [10]; (c) Wiegers *et al* [11]; (d) Matthews *et al* [12]; (e) Schaapman *et al* [13]; (f) Schwarz *et al* [14]. The magnetic field direction in (a) and (c)–(f) is vertical; in (b) it is horizontal. In all cases the normal to the plane of the 2DES is tilted by 15°–20° with respect to the field.

The torque caused by the magnetic moment of the 2DES caused an imbalance of the differential capacitor, which, connected to a ratio transformer, formed an ac voltage bridge. The magnetometer achieved a magnetic moment sensitivity of 10^{-12} J T^{-1} at 5 T, corresponding to an angular resolution of 10^{-7} rad. Assuming a maximum sample size of 3.5 by 3.5 mm, $R \approx 0.06\ \mu_B^*/e$.

In addition to the resolution defined above, two further figures-of-merit are useful for comparison of the performance of torque magnetometers. These are the angular sensitivity and angular responsivity; they are useful for comparing the geometries of different magnetometers (capacitor-plate configuration and dimensions) because they do not incorporate the effects of K. The angular sensitivity is defined as

$$S_\theta = \frac{1}{C}\frac{dC}{d\theta}, \qquad (1)$$

where C is the capacitance of one half of the differential capacitor when the deflection, θ, is zero. The angular responsivity, S_{out}, is defined as the output signal from the bridge for unit angular deflection. The angular responsivity is $dV/d\theta = (V_{\text{bridge}}/2C)\,dC/d\theta$ when the differential capacitor forms part of a voltage bridge, or $dI/d\theta = V_{\text{bridge}}\omega\,dC/d\theta$ when incorporated into a current bridge (ω the angular frequency of the bridge excitation). The design of any magnetometer is a compromise between attainment of high sensitivity, and stability of the instrument during thermal cycling. For experiments in which signals are relatively large (for instance those on induced currents, as discussed in section 3), it is prudent to use a thicker torsion fibre in order to ensure minimum movement of the magnetometer during cool-down. For the Eisenstein magnetometer $S_\theta = 2/\pi$; it is independent of deflection, so the instrument response is linear even at large angles. Thus, $S_{\text{out}} = V_{\text{bridge}}/\pi$.

Templeton [10] proposed an alternative magnetometer geometry consisting of a flat sapphire plate (rotor) suspended on a torsion fibre (37 μm diameter, 3 cm long, Mo–W wire), figure 1(b). The back side of the plate has a capacitance electrode evaporated on to it, and a pair of fixed capacitor plates are held parallel to it at a distance of 200 μm, forming a differential capacitor, whose imbalance is detected using an ac voltage bridge operating at 10 kHz. The 8 by 8 mm 2DES sample is attached to the front side of the sapphire plate and tilted so that the normal to the 2DES plane makes an angle of 20° with respect to the applied magnetic field. The magnet used was a horizontal bore split-coil superconducting solenoid; having the torsion fibre vertical has the advantage that there is no gravitational component to the restoring torque. The figures-of-merit for this instrument are: $S_\theta \approx l/2d$ (l the half-length of the rotor, d the separation of the capacitor plates), the approximation being for small deflections; $S_{\text{out}} \approx V_{\text{bridge}}l/4d$; and $R \approx 0.006\ \mu_B^*/e$. The angular sensitivity is about 27 times larger than for the Eisenstein instrument, though the resolution is only 10 times better. This may be because extraneous sources of mechanical noise are lower in the Eisenstein system, because the geometry of the Eisenstein instrument is better at decoupling from the mechanical noise, or because the resolutions quoted by the authors were for different measurement bandwidths. However the Templeton design clearly has potential for higher sensitivity, not least because its figures-of-merit depend on magnetometer parameters (rotor dimensions and plate separation) that can be optimized. A further advantage of the Templeton magnetometer is that applying a dc bias to one pair of capacitor plates produces a known torque which can be used to calibrate the instrument. The Templeton instrument becomes nonlinear at large deflections. This is rarely a problem in measurements of 2DES; furthermore, one can place the Templeton magnetometer within a feedback loop, in which the imbalance signal from the ac bridge provides a dc bias which rebalances the magnetometer, thereby minimizing magnetometer deflection and hence linearizing its response.

Wiegers *et al* [11] described a magnetometer whose design was optimized for low coupling to external sources of vibration. It consisted (figure 1(c)) of a 17.6 mm diameter, hollow, lightweight cylindrical rotor with eight capacitance electrodes evenly spaced around its outer diameter, and the 3 by 5 mm sample mounted on a platform at its centre. The rotor is suspended from 25 μm-diameter phosphor–bronze wires of overall length 10 mm, inside a cylindrical housing with eight pairs of capacitance electrodes around its inside perimeter. The gap between inner and outer electrodes is 0.2 mm. The symmetry of the rotor, with the suspension passing through its centre of mass helps reduce unwanted coupling to external vibrations. Furthermore, translations of the rotor along the two axes perpendicular to the suspension do not change the capacitances of the device to first order, resulting in further noise rejection. The figures-of-merit for this instrument are: $S_\theta = 16/\pi$; $S_{\text{out}} = 8V_{\text{bridge}}/\pi$; and $R \approx 0.03\ \mu_{\text{B}}^*/e$.

The present authors' magnetometer is described in [12] (figure 1(d)). It is similar to the Templeton design, but its rotor is of symmetric design, and includes a 'dummy' sample— a piece of GaAs substrate of the same dimensions as the 2DES—which cancels sources of background magnetization. It also uses a torsion fibre having rectangular section for greater stability and strength, and has *in situ* adjustment of capacitor-plate separation. It operates within the low-vibration environment of a sorption-pumped dilution refrigerator, attached to a 24-tonne concrete block suspended on air-springs. Normally our magnetometers are optimized for stability during thermal cycling; typical figures-of-merit are: $S_\theta \approx l/2d$, $S_{\text{out}} \approx V_{\text{bridge}}l/4d$ (as for the Templeton design); and $R \approx 0.01\ \mu_{\text{B}}^*/e$.

Schaapman *et al* [13] used an optical-lever detection method shown in figure 1(e). A 790 nm laser, optical fibre and spherical ball lens provided a collimated beam of light which was reflected from the back surface of the substrate of a 2DES, and into a quadrant detector. The quadrant detector, consisting of four optical fibres and four identical photodiodes located at room temperature, detects the small rotations of the 2DES with a resolution of 10^{-7} rad, resulting in $R \approx 0.01\ \mu_{\text{B}}^*/e$. The advantage of this method of detection is that it avoids exposing the 2DES to the large electric fields associated with capacitance detection. Exposure to stray infrared light is however a concern since it can influence both electron density and mobility [15].

Torsion-balance magnetometers can also be set up as torsional oscillators, in which the anisotropic component of magnetization causes a shift in the resonant frequency. Crowell *et al* [16] demonstrated this type of magnetometer, in which the rotor and torsion fibres were fabricated from a single piece of silicon, and were able to measure a magnetic moment of 2×10^{-11} J T^{-1} at 1 T using an averaging time of 10 s.

1.2. Cantilever torque magnetometers

Schwarz *et al* [14] have developed a cantilever magnetometer design, in which the cantilever and the frame to which it is attached are fabricated from the GaAs wafer containing the 2DES (figure 1(f)). This greatly reduces the background magnetization. The 2DES itself had dimensions 2 by 2 mm

and was positioned on a 'paddle' at the end of the cantilever. The thin part of the cantilever was 100 μm thick, 1 mm wide and 2 mm long. The quasi-static bending of the cantilever due to the $\boldsymbol{m} \times \boldsymbol{B}$ torque was measured; both capacitive and optical interferometric detection [17, 18] have been demonstrated. For capacitive detection, a magnetic moment as low as 5 $\times$ 10^{-15} J T^{-1} at 10 T, which is equivalent to $R \approx 0.002\ \mu_{\text{B}}^*/e$, was measured. Optical detection improves these figures by an order of magnitude.

Harris *et al* [19] have fabricated a GaAs micromechanical cantilever, length 320 μm, width 50 μm and thickness 0.1 μm incorporating a 100 μm by 40 μm 2DES. The cantilever was excited at resonance by a piezo-electric crystal and its motion detected using an optical-fibre interferometer. The magnetic moment of the 2DES produces an extra restoring torque which shifts the cantilever resonant frequency. The cantilevers had a resonant frequency of around 800 Hz with a quality factor Q of 30 000 in vacuum below 4.2 K. The resulting magnetic moment sensitivity was 3×10^{-17} J T^{-1} at 0.1 T, corresponding to $R \approx 0.005\ \mu_{\text{B}}^*/e$. Reducing the size of the 2DES by so much compared with torque magnetometry strongly reduces induced currents that otherwise can mask the dHvA oscillations. It also reduces the effects of long-range disorder. Because the sensitivity of a cantilever is inversely proportional to the cube of its thickness while the number of electrons in a 2DES scales as its area, it is beneficial to scale magnetometers down as long as a suitable detection scheme can be found.

2. Equilibrium magnetization

In 1930 de Haas and van Alphen [5, 20] discovered oscillations, as a function of magnetic field, in the low-temperature magnetization of the semi-metal bismuth. These oscillations are now usually referred to as the *dHvA effect*, or as *magnetic quantum oscillations* since they are intrinsically quantum mechanical in origin. The effect has been observed in many degenerate fermion systems, such as electrons or holes in a 3D or quasi-2D system, or even the more esoteric 'composite fermions' associated with the fractional quantum Hall effect (FQHE). It is closely related to the Shubnikov–de Haas (SdH) effect, in which the electrical resistance oscillates with field, and both phenomena are due to the Landau-level (LL) quantization [21–23] of allowed energy states of a charged particle in a magnetic field. Use of the dHvA effect as an experimental tool was pioneered by Shoenberg and extensively pursued by numerous researchers (see [24] for a detailed overview) in 3D systems. The dHvA effect in 3D systems proved a powerful method in the determination of the Fermi surface properties of metals as it yields not only the extremal Fermi surface cross-section (perpendicular to the field) but also electron scattering rates and effective masses. In contrast, the SdH effect (together with the Hall effect) has been more widely applied in obtaining similar information in 2D systems since in this case oscillations in resistance are fairly easily measured, whereas the magnetization oscillations are tiny because of the small number of charge carriers involved. However, because it is a thermodynamic rather than a transport property, the dHvA effect provides a far more direct quantitative measure of

Fermi surface properties and this has driven its theoretical and experimental application in 2D systems. Importantly, much of this work has also been driven by the desire to understand fully the physics of 2D systems in the quantum Hall regime.

The theory of the dHvA effect in 3D systems was developed to describe the observed oscillations in great detail, and the seminal theory of the non-interacting Fermi system is due to Lifshitz and Kosevich (LK) [25, 26]. Their theory yielded, as a Fourier-like series, an analytic expression for the oscillatory part of the magnetization as a function of magnetic field and temperature, including a treatment of spin-splitting. With the inclusion of the effects of electron scattering by impurities [27–29], this basic description was used in a vast range of Fermi surface studies of pure metals and alloys. It was later also extended to include the sometimes subtle modifications arising from many-body interactions [30–32]. However, the LK analysis cannot be quantitatively applied to 2D systems as various approximations which are made in its derivation break down: oscillations of the chemical potential μ, nearly always entirely negligible in 3D, are important in 2D systems [33] and in addition the approximation that the LL separation $\hbar\omega_c$ (discussed in 2.1.1 below) is small compared with μ commonly fails. Instead, since the early 1980s, new theoretical derivations of the 2D dHvA effect have been developed. Modified analytical formulae for the LK-type harmonics have been given by various authors, although these are less necessary with present-day computing power, which (given an underlying physical model) makes numerical evaluation of dHvA oscillations, and comparison with experiment, straightforward.

Experimentally, dHvA studies of 2D systems have grown following the increasing availability of high quality 2D systems. In this review we shall concentrate almost exclusively on the (quasi-) 2D electron system formed in gallium–arsenide-based heterostructures (mainly GaAs/(Al, Ga)As structures), where growth techniques have improved enormously since the 1970s, driven in great part by technological applications. Constraints of space, and the area of expertise of the reviewers, mean that we shall not consider much of the large body of important research carried out on quasi-2D systems such as intercalated graphite (see [34, 35] for reviews), organic charge-transfer salts [36] and rare-earth compounds.

2.1. Theory of the dHvA effect in 2D systems

The theory of magnetic quantum oscillations in a 2D Fermi system subject to a uniform magnetic field B, of magnitude **B**, perpendicular to its plane, differs in several respects from the 3D case. In 3D the dispersion of electron (or hole) energy in the z-direction (the direction of the magnetic field) is important: the LK formula shows that extremal areas of the Fermi surface cross-section perpendicular to z are responsible for dHvA oscillations, and that their curvature affects the magnitude and phase of the oscillations. The quasi-2D case is simpler since z-dispersion plays no role. (This simplicity is lost if more than the lowest subband of the 2D confining potential has to be included, and the 3D limit must of course be approached as the number of subbands is increased.) However, the 2D case

is complicated by the fact that, to maintain the number density of carriers constant, the influence of LL formation is to cause oscillations in the chemical potential μ [37–39, 33], as we describe shortly. In 3D these oscillations are negligible (much less than $\hbar\omega_c$) since changes in occupancy of the LLs are much smaller than the number of carriers enclosed by the whole Fermi surface. Additionally, many-body renormalization of the effective mass appearing in the LK formula has been shown [40, 41] to break down in 2D, unless the oscillations are significantly damped by thermal or scattering effects.

2.1.1. Landau levels and density of states. We first summarize the essential physics describing the dHvA effect, in the absence of spin-splitting and many-body effects. Consider a 2D system of electrons (occupying a single subband) having a quadratic zero-field dispersion relation $\epsilon(k) = \hbar^2 k^2 / 2m^*$ in an effective mass approximation where k is the in-plane wavevector $k = (k_x, k_y)$. The density of states (DOS) per unit area $\rho(\epsilon)$ is a constant $m^*/\pi\hbar^2$ (including spin degeneracy). The zero-field chemical potential μ_0 (often called the 'Fermi energy' or 'Fermi level') is determined by $\mu_0 \times m^*/\pi\hbar^2 = n_s$ where n_s is the number of electrons per unit area. In a magnetic field B in the z-direction the electron energy eigenvalues take the form (see (A.7))

$$\epsilon_\ell = \hbar\omega_c \left(\ell + \tfrac{1}{2}\right), \qquad (2)$$

where $\omega_c = eB/m^*$ is the cyclotron frequency. Each Landau level, labelled by the quantum number $\ell = 0, 1, 2, \ldots$ has, as shown in (A.9), a degeneracy g_L given by

$$g_L = 2eB/h, \qquad (3)$$

including spin. The DOS is thus split into a series of δ-functions separated by the energy $\hbar\omega_c$ and the number of LLs actually occupied is equal to n_s/g_L (n_s the 2D electron density), which can be non-integer. If spin-splitting of the levels is included, the degeneracy is halved and so this number is doubled to

$$\nu \equiv n_s h/eB \qquad (4)$$

which defines the *filling factor* ν. In terms of the *flux quantum* $\phi_0 \equiv h/e = 4.14 \times 10^{-15}$ T m^2, the filling factor is equal to the number of electrons in the sample divided by the number of flux quanta passing through the sample.

In a real system, perturbations result in a LL broadening Γ which is related to a scattering lifetime τ through the uncertainty relation $\Gamma \sim \hbar/\tau$. Hence the way in which the density of states deviates from the above ideal behaviour provides important information about the equilibrium properties of the 2DES. The most significant effect arises from electron–impurity scattering. In 3D systems, Dingle's phenomenological model [27] assumed that this scattering resulted in a Lorentzian broadening of each LL, an assumption later justified by Brailsford [28]. Brailsford's result appears not to transfer to 2D however, and over the years there has been no clear experimental or theoretical consensus as to the exact form of the DOS. An early theoretical paper by Ando and Murayama [42] examined

the broadening of LLs due to charged impurities, modelled as scatterers with a Gaussian potential, in a 2DES in a GaAs/(Al, Ga)As heterostructure including self-consistent screening. They concluded that the broadening is a strongly oscillating function of the position of the chemical potential, becoming largest when the μ lies between LLs and hence screening is minimized. Similar conclusions were reached on the basis of a number of calculations [43, 44] and experiments on heat capacity [45] and cyclotron resonance [46]. Smith *et al* [47, 48] modelled magnetocapacitance data using a field-independent Gaussian DOS, but a field-dependent width ($\Gamma \sim \sqrt{B}$) has also been reported experimentally from dHvA [9] and magnetocapacitance [49] measurements, the latter requiring in addition a constant background DOS. Other experiments though indicate a Lorentzian DOS [50, 51]. A more recent theoretical model of Glutsch *et al* [52] showed that a distorted Gaussian DOS can arise, which depends on LL index. We do not attempt to review all the seemingly conflicting data here, but restrict ourselves to examining, in section 2.2 some of the conclusions drawn from dHvA measurements by various authors.

To proceed further, we take two models of LL broadening which have been commonly employed, those of Lorentzian and Gaussian line shape. If each LL has a Lorentzian-shaped broadening, the resultant total density of states ρ_L can be expressed as

$$\rho_L(\epsilon) = \frac{2eB}{h} \frac{1}{\pi} \sum_{\ell=-\infty}^{+\infty} \frac{\Gamma}{(\epsilon - \epsilon_\ell)^2 + \Gamma^2}. \tag{5}$$

For mathematical convenience, this expression assumes that the sum over LLs can be extended to $-\infty$. One can then express the resultant periodic DOS as a Fourier series, which can be a convenient form for further calculation. This has been employed by Shoenberg [24] and Potts *et al* [51] in calculating magnetization (see also section 2.1.4 below). Although the true DOS does not extend below zero, this is expected to be unimportant since the oscillatory magnetization effects we consider below depend on the change of occupancy of states near the Fermi energy, which is usually much larger than both relevant energy scales Γ and $k_B T$. At the magnetic field at which dHvA oscillations just become resolved, $\hbar\omega_c \approx \Gamma$ but μ lies in a high-index LL so $\mu \gg \Gamma$ and $\hbar\omega_c$. In the extreme magnetic quantum limit ($\nu < 1$) $\mu \approx \hbar\omega_c/2$ but $\hbar\omega_c \gg \Gamma$ and $k_B T$.

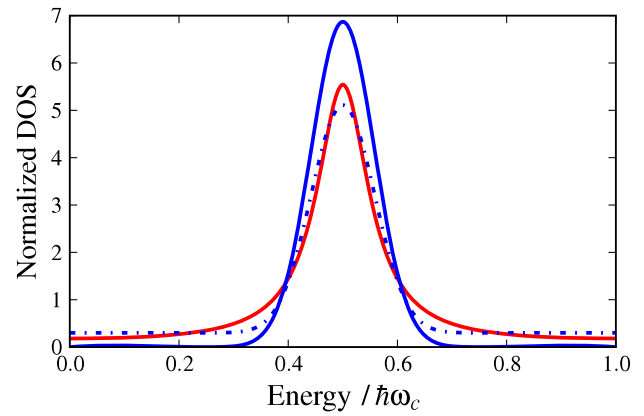Actually, (5) turns out to be summable in closed form [53]:

$$\rho_L(\epsilon) = \frac{2eB}{h} \frac{1}{\hbar\omega_c} \frac{\sinh\gamma}{\cos\beta + \cosh\gamma} \tag{6}$$

where γ and β are the dimensionless parameters

$$\gamma = 2\pi\Gamma/\hbar\omega_c \qquad \text{and} \qquad \beta = 2\pi\epsilon/\hbar\omega_c. \tag{7}$$

This equation takes simple forms in the weak scattering (or high-field) limit:

$$\rho_L(\epsilon) \approx \frac{2eB}{h} \frac{1}{\hbar\omega_c} \frac{\gamma}{1+\cos\beta}, \qquad \gamma \ll 1, \tag{8}$$

Figure 2. DOS around the lowest LL for Gaussian (10) (highest blue solid curve) and Lorentzian (5) (middle red solid curve) broadening with $\Gamma = 0.1$ meV. A value of $B = 1.0$ T has been chosen, corresponding to $\hbar\omega_c = 1.72$ meV for a gallium–arsenide-based heterostructure with electron effective mass 0.067 times the free electron mass. Also illustrated is a Gaussian with an added uniform background (blue broken curve) $\xi = 0.3$ as described by (26) discussed in section 2.2. The DOS have been normalized through division by the zero-field DOS.

and in the strong scattering (low-field) limit:

$$\rho_L(\epsilon) \approx \frac{2eB}{h} \frac{1}{\hbar\omega_c} (1 - 2e^{-\gamma}\cos\beta), \qquad \gamma \gg 1, \tag{9}$$

which tends to the expected zero-field value $m^*/\pi\hbar^2$ as $\gamma \to \infty$. The above equations (8) and (9) are useful in obtaining analytic expressions for the magnetization.

A Gaussian broadening leads to a total density of states ρ_G that can be expressed as

$$\rho_G(\epsilon) = \frac{2eB}{h} \frac{1}{\Gamma\sqrt{2\pi}} \sum_{\ell=-\infty}^{+\infty} \exp\left[-\frac{(\epsilon - \epsilon_\ell)^2}{2\Gamma^2}\right] \tag{10}$$

where again the sum over LLs has been extended to $-\infty$. This summation does not, as far as we are aware, have a convenient closed-form expression. However, it is easily evaluated numerically by summing over a few LLs around ϵ since the exponentially decreasing tails of the Gaussians give rapid convergence. Alternatively this periodic DOS can again be written as a Fourier series.

The shapes of these DOS are illustrated in figure 2.

2.1.2. Thermodynamics. We next require an expression relating the magnetization to thermodynamic properties of the system. This follows simply from the expression $-m\,dB$ for the work done on a sample of magnetic moment m when the external field is increased by an amount dB (we take m and B parallel for simplicity). Then the change dU in internal energy of the sample can be written with usual notation as

$$dU = T\,dS - m\,dB \tag{11}$$

if volume changes are neglected. However, it is more usual to consider an 'open' system, in which the number of particles is not fixed, in which case (11) is modified to read

$$dU = T\,dS - m\,dB + \mu\,d\mathcal{N}, \tag{12}$$

where the last term allows for change in the particle number $\mathcal{N}$, and μ is the chemical potential. The reason for taking an open system only becomes apparent when looking at the statistical mechanics of the problem; it turns out to be mathematically much simpler [54] to evaluate the grand canonical partition function instead of the canonical partition function. (This mathematical convenience of course has no influence on the physics, as is clear by imagining the open system just to be a subsystem in a much larger closed system.)

Introducing the Helmholtz free energy defined by $F \equiv U - TS$, and the thermodynamic potential defined by $\Omega \equiv U - TS - \mu\mathcal{N}$, it follows that we can write m in either of the forms

$$m = -\left.\frac{\partial F}{\partial B}\right|_{T,\mathcal{N}} \qquad \text{or} \qquad m = -\left.\frac{\partial \Omega}{\partial B}\right|_{T,\mu}. \qquad (13)$$

It is also useful to derive the following equations from (12):

$$\mu = \left.\frac{\partial F}{\partial \mathcal{N}}\right|_{T,B} \qquad \text{and} \qquad \mathcal{N} = -\left.\frac{\partial \Omega}{\partial \mu}\right|_{T,B}. \qquad (14)$$

These thermodynamic relations are quite general, and as pointed out by Shoenberg [24] for example and many others, one may use *either* formula (13) to evaluate m, depending on which is more convenient: any physical constraint, such as a fixed number of particles or fixed electrochemical potential, or even something in between, must still be built into the evaluation of F or Ω. Indeed, magnetic quantum oscillations in a 2D system are qualitatively rather different in the limits of a constraint of fixed carrier number density n_s (equal to $\mathcal{N}/A$ where A is the sample area) or fixed chemical potential μ. (As already noted, the difference in 3D systems is usually small enough to ignore.) In fact, for a single subband the zero temperature, zero-scattering, ideal sawtooth oscillations in m are of opposite sign for the two cases, while for a multi-subband system extra oscillation frequencies are produced if n_s is fixed.

2.1.3. Statistical mechanics. The central quantity of statistical mechanics for an open system is the grand canonical partition function Ξ, which is related to the thermodynamic potential Ω by

$$\Omega = -k_B T \ln \Xi. \qquad (15)$$

For a gas of independent fermions with single-particle eigenenergies labelled ϵ_i it can be shown [54] that

$$\ln \Xi = \sum_i \ln[1 + e^{(\mu - \epsilon_i)/k_B T}]. \qquad (16)$$

It thus follows from the second equation in (14) that

$$\mathcal{N} = \sum_i [e^{(\epsilon_i - \mu)/k_B T} + 1]^{-1}. \qquad (17)$$

In terms of the DOS these become

$$\Omega = -k_B T \int \rho(\epsilon) \ln[1 + e^{(\mu - \epsilon)/k_B T}] \, d\epsilon \qquad (18)$$

and

$$\mathcal{N} = \int \rho(\epsilon)[e^{(\epsilon - \mu)/k_B T} + 1]^{-1} \, d\epsilon. \qquad (19)$$

The free energy F is therefore just

$$F = \mu\mathcal{N} - k_B T \int \rho(\epsilon) \ln[1 + e^{(\mu - \epsilon)/k_B T}] \, d\epsilon. \qquad (20)$$

From the energy eigenstates of 2D electrons as a function of magnetic field, the thermodynamic quantities Ω and F, and hence the magnetic moment, may be evaluated. In certain limits of $\hbar\omega_c$, μ and $k_B T$ useful analytic approximations to m can be made. However, the equations are most easily evaluated numerically (and this is essential in comparing with experimental results), so we first look at some simple numerical illustrations.

2.1.4. Some simple examples. If the electrochemical potential μ were fixed, the integration in (18) could be performed directly numerically as a function of field, and the resultant Ω differentiated with respect to B as in (13). For a 2D system it is usual to assume that the electron density n_s is fixed, independent of magnetic field (possible departures from this picture will be examined later). This means, by (14), (17) or (19), that μ is field dependent and needs first to be evaluated at each field value before calculating Ω or F. (Zawadzki [55] followed essentially this procedure in an early model of 2D dHvA, but assumed a delta function DOS.) The general procedure used for fixed $\mathcal{N}$ is thus as follows: (i) calculate μ from (19), using an iterative method such as bisection [51]; (ii) find Ω and hence F using (18) and (20); (iii) differentiate F with respect to B to find m (13). Alternatively, it is possible to replace steps (ii) and (iii) by differentiating Ω numerically *at constant* μ, but this requires twice the number of evaluations as the first method.

The above is illustrated by looking at the case of an idealized 2D electron system at zero temperature and with no LL broadening, calculated numerically as described above and shown in figure 3. The periodicity of the oscillations is straightforward to understand: taking $T = 0$ the occupancy of the LLs is such that $n_s = g_L(\ell_{max} + f)$, where ℓ_{max} is the index of the highest occupied LL and the fractional occupancy f of the highest LL (in the range 0–1) maintains constant total number density. Thus $\ell_{max} = \text{trunc}(n_s/g_L)$, where $\text{trunc}(x)$ is the largest integer value less than or equal to x. As g_L increases with increasing field, ℓ_{max} becomes smaller; f drops to zero periodically in reciprocal field whenever
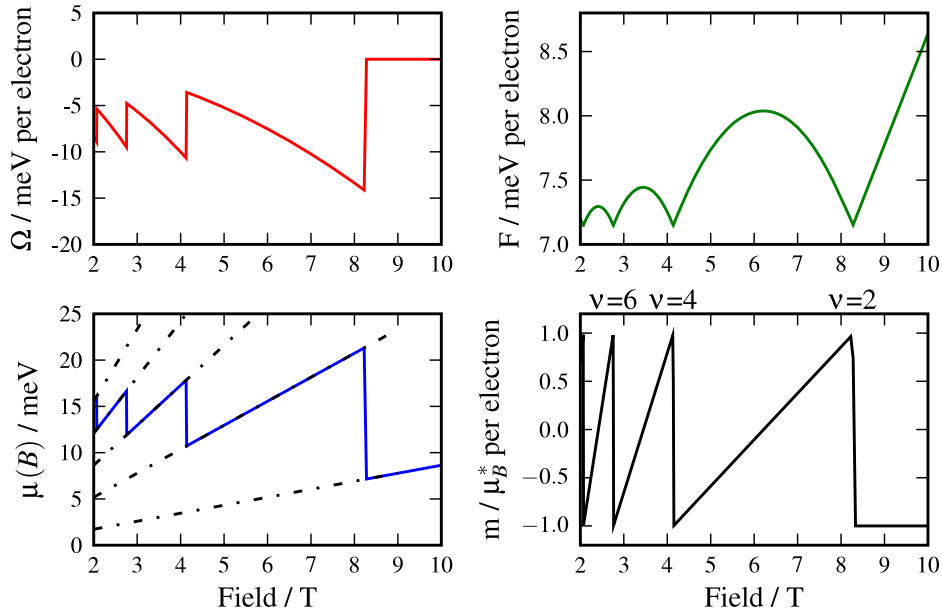
$$\frac{1}{B} = \frac{2e}{h n_s} \ell_{max} \qquad (21)$$

and so the number density can be measured from the oscillation period. The quantity $h n_s/2e$ is the dHvA frequency.

The free energy is the sum of the individual LL energies

$$F = U = g_L \hbar \omega_c \left[\sum_{\ell=0}^{\ell_{max}-1} (\ell + \tfrac{1}{2}) + f(\ell_{max} + \tfrac{1}{2}) \right]$$
$$= g_L \hbar \omega_c [\tfrac{1}{2}\ell_{max}^2 + f(\ell_{max} + \tfrac{1}{2})].$$

Figure 3. Theoretical thermodynamic potential Ω, free energy F, electrochemical potential μ and magnetic moment m versus field for a GaAs 2DES with number density 4×10^{15} m^{-2}. The broken lines on the graph for μ show the field-dependent energies ϵ_ℓ of the lowest Landau level $\ell = 0$ (lowest slope) and the levels $\ell = 1 \cdots 4$ as given by (2). The temperature and broadening are both set to zero.

Differentiation of F, bearing in mind that ℓ_{max} is stepping with field, gives m. The sawtooth shape of the magnetic moment oscillations at $T = 0$ reflects a gradual rise of $\mu = (\ell_{max} + \frac{1}{2})\hbar\omega_c$ with increasing field, followed by its instantaneous drop when the highest partially filled LL becomes empty, as seen in the graph for μ in figure 3. The highest LL is partially occupied, except at the lowest points on the μ curve, and its occupancy decreases as the field is raised. The maximum excursion of the oscillations from $m = 0$ in this case is one effective Bohr magneton per electron (the effective Bohr magneton $\mu_B^* = e\hbar/2m^* = 1.38 \times 10^{-22}$ J T^{-1} in GaAs, where the electron effective mass is 0.067 times the free electron mass). This follows since, at zero T, the jump Δm in magnetic moment (per electron) will be $\sim \hbar\omega_c/B = 2\mu_B^*$.

If LL broadening is included, the amplitude of the dHvA oscillations is damped by a field-dependent factor approximately as $\exp(-2\pi\Gamma/\hbar\omega_c)$. Physically, the broadened DOS smears out the change in LL occupancy if $\Gamma \gtrsim \hbar\omega_c$. Similarly, the influence of finite T is to cause the amplitude of the dHvA oscillations to depend on field and temperature roughly as $\exp(-2\pi^2 k_B T/\hbar\omega_c)$. This occurs due to $k_B T$ broadening of the Fermi function in (20) which smears out the change in LL occupancy if $k_B T \gtrsim \hbar\omega_c$. An exact numerical calculation of the effect of temperature is shown in figure 4.

We examine numerically the effect of LL broadening shortly, and compare with experimental results in section 2.2, but it is first instructive to look at an analytical approximation. The amplitude reduction factor due to scattering follows straightforwardly from (9), valid in the limit $2\pi\Gamma \gg \hbar\omega_c$. Substituting (9) into (19) for the particle number, the oscillatory part of $\mathcal{N}$ contains the factor $\exp(-2\pi\Gamma/\hbar\omega_c)$ and can be neglected, yielding μ approximately constant $(m^*/\pi\hbar^2)\mu \approx n_s$. (This is of course the approximation appropriate to the derivation of the LK formula in 3D, and
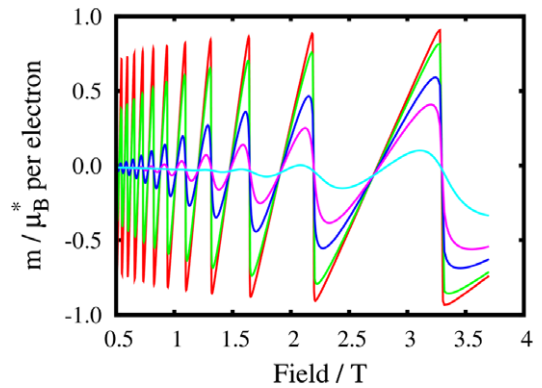
Figure 4. Theoretical magnetic moment m versus field for a GaAs 2DES with number density 3.18×10^{15} m^{-2}, at temperatures of 0.3, 1, 3, 5 and 10 K.

hence we expect the LK formula to become valid in 2D in this limit. In general though, departures from the LK harmonics will be seen in 2D [56].) Substituting (9) into (18) yields, since the first term in an integration by parts vanishes,

$$\Omega = -\frac{2eB}{\pi h} e^{-\gamma} \int_0^\infty \frac{1}{1 + e^{(\epsilon - \mu)/k_B T}} \sin\left(\frac{2\pi\epsilon}{\hbar\omega_c}\right) d\epsilon$$

where we have dropped the term which is not oscillatory in field. The lower limit of integration can be extended[3] to $-\infty$ without changing the oscillatory part of the integral, if $\mu \gg k_B T$, and it is then easily evaluated using a suitable contour integration to give

$$\Omega = \frac{2eB}{h} k_B T \frac{\exp(-2\pi\Gamma/\hbar\omega_c)}{\sinh(2\pi^2 kT/\hbar\omega_c)} \cos\left(\frac{2\pi\mu}{\hbar\omega_c}\right). \quad (22)$$

[3] A factor $\exp(-\delta|\epsilon|)$, $\delta \to 0$ must be introduced to ensure convergence of the integral.
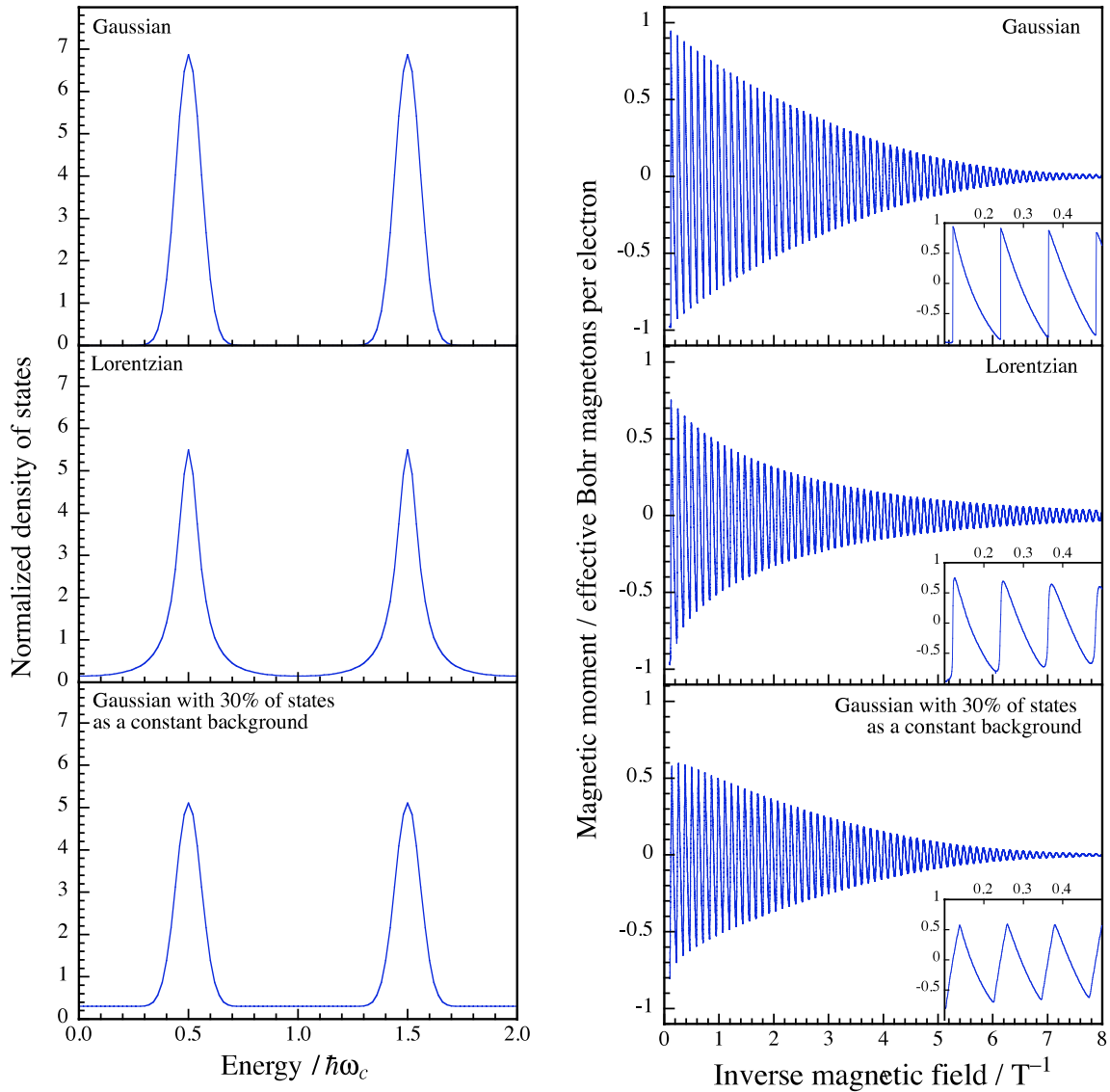
Figure 5. Model densities of states (for $B = 1$ T) (left) and the resulting dHvA oscillations versus inverse magnetic field (right) for a 2DES with $n_s = 4 \times 10^{15}$ m^{-2}, broadening parameter $\Gamma = 0.1$ meV, at a temperature of 0.05 K. The DOS models are, from top to bottom, a Gaussian (10), a Lorentzian (5) and a Gaussian with an added constant background with $\xi = 0.3$ (26). The damping of the oscillations is clearly different for the three models. The insets show a few high-field oscillations: the Gaussian DOS gives near-ideal sawtooth oscillations, while the Lorentzian is significantly smoother and smaller than ideal. The introduction of a background skews the sawtooth as well as reducing the amplitude.

The sinh term is $\sim \exp(-2\pi^2 kT/\hbar\omega_c)$ in the high-temperature limit.

The low-temperature limit is not amenable to a simple analytic formulation, so we consider a few illustrative numerical calculations in figure 5. This shows the effects of different model DOS on the dHvA oscillations in the low-field limit $k_B T \ll \Gamma$. For a Gaussian DOS, the oscillation amplitude of ± 1 effective Bohr magneton per electron in the high-field limit is reached more quickly than for the Lorentzian DOS, and consequently the sawtooth shape (insets to right-hand panels) is more pronounced in the former case. Addition of a constant background DOS reduces the dHvA oscillation amplitude and also skews the sawtooth shape seen at high field (inset to bottom right-hand panel).

2.1.5. Many-body interactions. In principle, electron–electron and electron–phonon scattering need to be included in the dHvA effect. In 3D, many-body generalizations of the LK formula exist. The case of electron–electron interactions was shown by Luttinger [30] merely to alter the phase of the oscillations. Electron–phonon interactions were treated by Engelsberg and Simpson [31] for a realistic phonon spectrum and revealed the surprising result that almost the only effect is to renormalize the effective mass in the LK expression, rather than to contribute to LL broadening through electron–phonon scattering—a result confirmed by experiment [57]. (Small departures from the LK formula were also predicted and later confirmed experimentally [32, 58].)

The above treatments used in 3D are not directly applicable to the 2D case: for electron–electron interactions

Curnoe and Stamp [40] showed that, depending on conditions of temperature and scattering, there would be very strong departure from the LK formula. This is a result of the breakdown of an expansion in $\hbar\omega_c/\mu$ of the electron self-energy which is valid in 3D only [30]. Martin *et al* [41] included the effects of disorder and interactions in 2D, with the approximation that oscillations in μ were small. They found that the dHvA oscillations will follow the field and temperature dependence of the LK formula, valid in 3D, only if the oscillations are heavily damped by the disorder or temperature. They also noted that, similar to the 3D case, any inelastic interactions, electron–phonon or electron–electron, do not damp the oscillation amplitude, although they do renormalize the effective mass. Finally, they found that accounting for interference between electron–impurity and electron–electron interactions resulted in a temperature-dependent effective mass scaling as $T \ln T$. This last result was confirmed by calculations of Adamov *et al* [59] and there is supporting experimental evidence for it [60–62] in SdH studies.

2.1.6. Relationship with edge currents. Although (in a macroscopically-sized sample) the dHvA effect is a bulk equilibrium thermodynamic effect and can be quantified without regard to the boundaries of the real, finite, sample (see for example the book by Peierls [63] for a short history) it is instructive briefly to examine the magnetization from the complementary viewpoint of equivalent currents flowing around the edge of the sample. (In samples where the lateral dimension become comparable with the magnetic length l_B, as discussed in section 2.2.6, the boundaries of course play an important role.)

If the magnetization M is the magnetic moment per unit area (restricting the treatment to 2D, M has units of ampere) we can relate this to Amperian equivalent currents using standard electromagnetic theory [64]. The equivalent current density (in A m^{-1}) in the bulk is

$$j_{\text{bulk}}(r) = \nabla \times M. \tag{23}$$

The bulk current is thus zero for a homogeneous sample which has uniform magnetization. The current (in A) flowing around the sample edge is

$$I_{\text{edge}} = M \times n \tag{24}$$

where n is the outward unit vector in the 2D plane normal to the sample edge. In terms of current density this can be expressed

$$j_{\text{edge}} = M \times n \, \delta(r - r_{\text{edge}}). \tag{25}$$

The physical interpretation of the last equation is that a uniform magnetization M can be replaced by an equivalent current flowing around only the outermost edge of the sample.

The above three equations are general and apply classically or quantum mechanically. However the relationship with the current carried by particular quantum states in the bulk or near the edge of a sample is not always straightforward. As noted by Středa and Smrčka [65], the
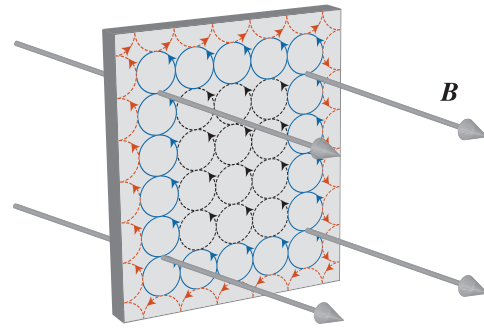
Figure 6. Highly schematic representation of the cyclotron orbits of electrons in a rectangular 2DES. The (black dashed) inner orbits in the bulk of the sample combine with the (blue solid) skimming orbitals to produce a counterclockwise conventional current. The (red dashed) skipping orbits produce a clockwise conventional current. Classically these two currents exactly cancel, but in a quantum mechanical picture they do not.

thermodynamic equilibrium edge currents which give rise to electron diamagnetism of free electrons can usefully be thought of (for macroscopic samples) as divided into two classes: (i) skimming currents, where the cyclotron orbits lie within the bulk of the sample; and (ii) skipping currents, which are associated with cyclotron orbits interrupted at the surface and which therefore travel along the edge in the opposite direction to bulk orbits. These orbits, together with bulk orbits, are illustrated for the classical case in figure 6. Classically, M is zero as the skimming and skipping currents exactly cancel, but this cancellation is not generally exact in a quantum mechanical calculation. Bremme *et al* [66] presented a simple picture of non-interacting electrons without scattering to show the contributions to the magnetic moment of the sample arising from both bulk (including skimming) and skipping states in the quantum mechanical case. They verified that the magnetic moment of equilibrium bulk currents arise from currents flowing near the sample edge.

How do these edge currents relate to the well-known edge state picture [67] used to describe the quantum Hall effect? There are several points to note: first, the edge states of the QHE correspond to the classical chiral skipping orbits described above; second, the oscillatory magnetic moment depends on currents due also to skimming orbits; third, the QHE describes a *non-equilibrium* situation in which electron states acquire a drift velocity due to the influence of the Hall electric field. As we touch on later in section 3.4, when electron–electron interactions and impurity scattering are taken into account these simple pictures of the current distribution are substantially altered.

2.2. Experimental results

Not long after the availability of semiconductor-based 2D electron systems, attempts were made to examine magnetic quantum oscillations. Störmer *et al* [1] reported the first observation of the dHvA effect in such a system in 1983. They employed a SQUID magnetometer to examine a modulation-doped GaAs/(Al, Ga)As heterostructure at 1.5 K, but needed to

stack 4000 layers and used extremely slow acquisition rates to obtain sufficient signal-to-noise ratio. Sample inhomogeneity, leading to a phase broadening, was invoked to explain the size of signal observed, which was much smaller than the ±1 effective Bohr magneton per electron predicted by theory for an ideal system. In the same year, Fang and Stiles [68] reported dHvA oscillations in a silicon inversion layer in fields up to 15 T. As was standard in measurements on 3D systems at that time, they detected the magnetic moment m of the sample using an inductive pick-up coil. This was placed above the periphery of the gate electrode of a metal-oxide-semiconductor field-effect device. Modulation of the gate voltage, and hence n_s, at frequencies up to 100 kHz gave a change in m, and hence the magnetic flux linking the coil, inducing a measurable voltage observed as peaks at certain values of n_s. These spikes were interpreted as the derivative of m with respect to n_s. In fact, improved SQUID magnetometry with gate voltage modulation was developed by Meinel *et al* [2] in 1997, so that a single-layer GaAs/(Al, Ga)As structure could be examined. However potential complications of modulation techniques (capacitive coupling, the requirement of sample gating, and induced currents in the 2DES—see section 2.2.5) and the lack of sensitivity of the SQUID method for magnetic moment detection led to more direct methods being employed. Also key to developments in this field was the increasing availability of high quality 2DES.

Eisenstein *et al* [8, 6, 9, 69] were the first to employ torque magnetometry (see section 1.1 for further details of magnetometer design), with capacitive detection of the sample motion, to analyse dHvA oscillations from GaAs/(Al, Ga)As superlattice samples and a single-layer heterojunction, at 4 K in fields up to 10 T. The idealized sawtooth-like dHvA waveform was not seen in their samples, which had Hall mobilities, μ_H, less than 8 m^2 V^{-1} s^{-1} for the superlattices and 28 m^2 V^{-1} s^{-1} for the single layer, but nevertheless quantitative information could be extracted from the field dependence of the (roughly sinusoidal) dHvA oscillations. They reported that the observed oscillation envelope implied a Gaussian DOS with a field-dependent broadening parameter Γ scaling as $\sqrt{B}$, but they did not give details of their fitting procedure.

The torsion magnetometer technique was improved by Templeton [10], who examined a GaAs/(Al, Ga)As heterostructure with $n_s = 9.1 \times 10^{15}$ m^{-2} and $\mu_H = 8$ m^2 V^{-1} s^{-1} at 4.2 K. The oscillations were again roughly sinusoidal, characteristic of a small quantum lifetime, but the amplitude approached 50% of the theoretical maximum at 4 T in contrast with the findings of Eisenstein *et al*. Without further studies, it is not clear if this was a true sample-dependent effect or whether it was caused by difficulties in calibrating the earlier magnetometers. The field dependence of the oscillations was again used to extract an estimate of the DOS, and a Gaussian broadening $\Gamma = 0.85$ meV (around 10 K) without a $\sqrt{B}$ dependence was found to fit the data well. This corresponds to a quantum lifetime of about 0.8 ps compared with the momentum relaxation time (the lifetime related to the mobility μ_H measured in transport) of 3 ps.

Similar designs to Templeton's, with various improvements such as *in situ* adjustment and a balanced rotor, were

used extensively in later studies of the dHvA effect by the present authors [51, 70–72]. Potts *et al* [51] were the first to present a detailed numerical fitting procedure to analyse dHvA oscillations. Data taken from a 10-layer 2DES ($n_s = 1.2 \times 10^{16}$ m^{-2} and $\mu_H = 2.9$ m^2 V^{-1} s^{-1}) yielded a best fit to a model DOS which was Lorentzian in shape with a width $\Gamma \sim 2.5$ meV, or nearly 30 K, that was independent of B. (Interestingly, unlike suggestions in some other experiments, discussed later, the best fit was obtained with no background DOS included.) The Gaussian form with width proportional to $\sqrt{B}$ only gave a good fit at low fields. Some evidence for a temperature dependence of Γ was seen over the range 0.1–4.2 K examined.

It is of course essential to a proper understanding of the thermodynamic DOS in a 2DES to examine samples with a *range* of mobilities, and in 1997 Wiegers *et al* [73] examined, amongst other samples, a high-mobility ($n_s = 2.3 \times 10^{15}$ m^{-2}, $\mu_H = 230$ m^2 V^{-1} s^{-1}) single-layer GaAs/(Al, Ga)As heterojunction which showed a dHvA effect at 1.2 K approaching the idealized sawtooth oscillations of figure 3. Only a semi-quantitative analysis was attempted on the relatively noisy data, but it was clear that the LL broadening, of whatever form, was much smaller than in previous samples, probably around 6 K.

Using cantilever-based magnetometry (see section 1.2), Schwarz *et al* [74, 75] reported an impressive set of dHvA measurements on two samples, with $n_s = 5.8 \times 10^{15}$ m^{-2}, $\mu_H = 40$ m^2 V^{-1} s^{-1} and $n_s = 4.8 \times 10^{15}$ m^{-2}, $\mu_H = 140$ m^2 V^{-1} s^{-1}. They examined the temperature range from 0.3 to 30 K. The lower-temperature data also showed induced eddy current peaks. The high mobility (and about a factor 100 smaller sample sizes, ~2 mm^2, which will reduce the effects of sample inhomogeneity) again resulted in almost ideal dHvA oscillations, with amplitude approaching ±1 effective Bohr magneton per electron. They reported that the amplitude of the dHvA oscillations as a function of field agreed with the Dingle formula; but since this formula is based on a model of a Lorentzian DOS and applies to the fundamental harmonic component alone, one should be extremely cautious in using it for quantitative analysis. (It may nevertheless be a reasonable approximation when $k_B T$ and/or Γ are comparable with $\hbar\omega_c$.) However, as we shall discuss shortly, they also performed a quantitative analysis in which they were able to fit the oscillations with a DOS consisting of a sum of a Gaussian, with Γ varying as $\sqrt{B}$, and a *field-dependent* background term. In a similar vein, Zhu *et al* [71] (using torsion-balance magnetometry on large-area samples) also obtained sawtooth-like dHvA in their two samples ($n_s = 4.4 \times 10^{15}$ m^{-2}, $\mu_H = 50$ m^2 V^{-1} s^{-1} and $n_s = 3.1 \times 10^{15}$ m^{-2}, $\mu_H = 78$ m^2 V^{-1} s^{-1}) examined from 0.05 to 1 K. The work of both groups showed that the sawtooth did not quite have the dramatic asymmetric shape of figure 3 with a sharp jump on the high-field side of each sawtooth, but instead had a noticeably finite slope. To explain this, both Schwarz and Zhu considered a background DOS between LLs, that is, a density of states

$$\rho(\epsilon) = \xi \frac{m^*}{\pi\hbar^2} + (1 - \xi)\rho_{L/G}(\epsilon), \qquad (26)$$
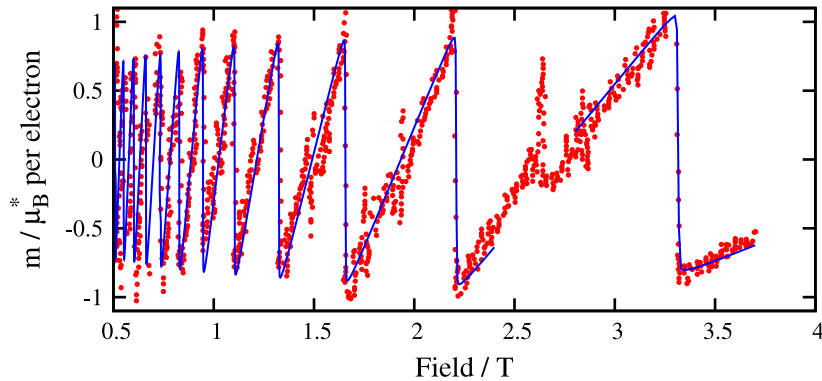
Figure 7. Comparison between theoretical magnetization (solid line) for a Lorentzian DOS $\Gamma = 0.05$ K with no background, and experimental data from reference [77] figure 6. The number density chosen was $n_s = 3.20 \times 10^{15}$ m^{-2}. As in reference [77], the theory has been adjusted at higher fields to correct for the influence of an eddy current peak around 2.6 T.

where the first term is an energy-independent background DOS and the second term represents the remaining Lorentzian or Gaussian-broadened LLs as in (5) and (10) (see the bottom left panel of figure 5). (A Gaussian-plus-constant DOS was suggested by Gornik *et al* [76] to explain heat capacity measurements in samples of comparatively poor mobility.) The quantity ξ parametrizes the fraction of states between LLs. Zhu *et al* [71] used a full fitting procedure (a development of the method of Potts *et al* [51]) to reproduce accurately their experimental results, using the broadening Γ and background ξ as the main adjustable parameters. They deduced that either a Lorentzian or a Gaussian DOS would fit the results equally well, with broadening around 0.2 or 0.3 eV, as long as the background term ξ was included. This varied from 0.14 to 0.49, depending on sample conditions, for the case of a Gaussian DOS, and 0.0–0.28 for the Lorentzian. The smaller value in the latter case reflects the greater intrinsic spread of a Lorentzian. In contrast, Schwarz *et al* [75] reported best fits to their data with a field-dependent Gaussian broadening, $\Gamma = 0.08$ meV$\sqrt{B}$ with B in tesla, and also deduced that the background term was proportional to filling factor ν (inversely proportional to field) with values of $\xi \sim 2.3 \times 10^{-2} \nu$. They interpreted this as evidence of the influence of edge states in their samples.

How should one interpret these apparently contradictory conclusions about the DOS? A mundane explanation is simply that the data are not always sufficiently good to extract the DOS accurately. A more interesting possibility is that high-mobility samples can indeed show different DOS depending on sample growth or on experimental conditions. An attempt to explore these possibilities was made by Usher *et al* [72] who performed an analysis of Zhu's data using both DOS models. For that data set at least, they concluded that to get the best fit over a wide field range a *constant* value of ξ with a field-independent Gaussian broadening Γ was required. It was also pointed out that fits were made over a much larger number of dHvA oscillations in the data of Zhu *et al* compared with the data of Schwarz *et al* (ten or twenty oscillations versus five) and this is crucial in deciding between different DOS models: a stringent requirement on the fit is that it can reproduce the dHvA envelope over a large change in amplitude.

A recent work of Wilde *et al* [77] extends and supports the earlier findings of Schwarz. They present dHvA data from three samples of varying mobility ($\mu_H = 70$, 140 and 900 m^2 V^{-1} s^{-1}) at a temperature of 0.3 K showing comparisons with theory for a $\sqrt{B}$ Gaussian DOS with ν-dependent background. In all cases they show convincing agreement with experiment. However even here it is not clear that the data, which are among the best available in the literature, can be used to argue for a particular DOS model. For example, in figure 7 we show a comparison of their published dHvA data in the high-mobility sample (sample bo# 1121 in their figure 6) and theory using a Lorentzian DOS, with no background states included. Evidently the fit with the data is quite comparable to their alternative DOS model. For this sample its very high quality means that virtually any sufficiently narrow broadening function will fit the data, and the effect of $k_B T$ is dominant. However, we find that a Lorentzian also fits data from the other, lower mobility, samples equally well. To distinguish between the models, measurements extending to lower field where the envelope of the oscillations becomes smaller would be useful. In other words, it is advantageous to measure with the cyclotron energy $\hbar\omega_c$ ranging from greater than to rather less than Γ. For a sample of such high quality ($\Gamma \sim 0.05$ K assuming Lorentzian broadening) this is completely impractical, requiring such small fields that torque magnetometry is not viable. However, it would be practical instead to examine the temperature dependence of the oscillations for $k_B T$ covering this energy range.

It seems that there are quite subtle differences, at least in terms of their influence on magnetization, in the overall DOS produced by some apparently quite different models. Two avenues of research are clearly required: firstly, theoretical justification of these models, which is lagging behind their eager uptake by experimentalists, needs to be improved. Secondly, to decide experimentally between the competing pictures it is vital to see further measurements which cover a systematic range of sample mobilities and are made over the widest possible range of field and (in particular) temperature.

Usher *et al* [72] also suggested an alternative explanation for the finite high-field slope of the sawtooth oscillations they

observed: only if the 2DES is completely isolated, so that its density cannot change in response to the changing magnetic field, is n_s fixed and the idealized oscillations take the sawtooth form. This possibility has been considered by several authors in the past [78–80]. If n_s itself were allowed to oscillate with field, the high-field slope would become finite. The extreme case of this would be a fixed chemical potential, independent of field, which would produce sawtooth dHvA in which the *low-field* jumps are abrupt [81]. It was hypothesized that a real system is somewhere between these two limits. We discuss this idea further in section 2.2.3.

Zhu *et al* [71] additionally examined the effect of illuminating their samples with a red light-emitting diode, which is known to increase the number density and mobility of the 2DESs, due to persistent photoconductivity. After illumination both samples displayed these expected increases, and in a δ-modulation-doped sample this was accompanied by a commensurate reduction in the LL broadening deduced from dHvA. However, surprisingly, the bulk modulation-doped sample showed an *increase* in width after illumination. In fact, as Zhu *et al* pointed out, this is not actually a counter-intuitive result: firstly, it has been known for many years that the *transport* and *quantum* lifetimes measured by the Hall and dHvA effects respectively are very different [82]. Secondly, it underlines the fact that extended and localized states in these systems in general sample the disorder in very different ways—thus even a comparison of the quantum lifetime from dHvA and SdH oscillations do not necessarily agree. In Zhu's case the illumination reduced the disorder experienced by the extended states (which are the only ones influencing the transport mobility) while increasing that experienced by the localized states (to which dHvA measurements are also sensitive). The results of Ruhe *et al* [18] also point to the non-equivalence of these lifetimes, but further show that the differences can be quite extreme: by varying sample density with a gate and measuring transport and dHvA in the *same* sample they showed that the dHvA amplitude can be almost unaffected even as μ_H is varied from 10 to 50 m² V⁻¹ s⁻¹. However, they assert that the quantum lifetime in dHvA should 'not be interpreted as a scattering time of electrons at the Fermi energy as is done in the case of SdH' but that it is a 'measure for the broadening of the Landau levels and considers all occupied levels'. In fact both dHvA and SdH oscillations are governed by change in occupancy of electrons around a *range* $k_B T$ or $\hbar\omega_c$ about μ; it is the distinction between extended and localized states that underlies the difference between dHvA and SdH quantum lifetimes.

2.2.1. Sample inhomogeneity. Although an intrinsic DOS has been most commonly used to explain the shape and field dependence of dHvA oscillations, sample inhomogeneity could be important, particularly in high-mobility samples. Similar ideas have been used in the past to describe apparent LL broadening observed in 3D systems [24, 83, 84]. The simplest model is that of a sample comprising a number of *independent* portions of slightly different number density, each of which contributes to the total dHvA magnetic moment. (Thus the number density in each region is constant and μ
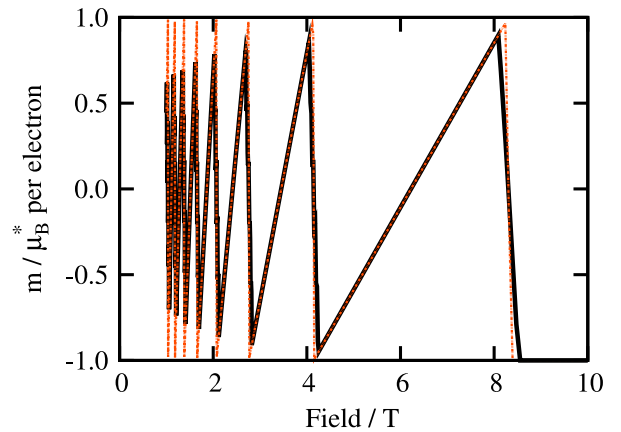
Figure 8. Total dHvA magnetic moment versus field (solid black curve), for zero temperature and no scattering, of a GaAs 2DES comprising five regions differing by ±1% and ±2% centred on a density 4.00×10^{15} m⁻², as for figure 3. A finite width of the downward jumps of magnetization is produced compared with a single n_s (broken red curve), as well as a reduction in amplitude. The curve becomes smoothed out as more regions are considered.

will oscillate independently in each region.) To illustrate this, figure 8 shows the total magnetic moment of an otherwise perfect sample (at zero temperature) of five equal regions with n_s differing by just ±2%. A finite high-field slope of the sawtooth oscillations is thus consistent with a small sample inhomogeneity. A further consequence is a field-dependent damping of the oscillation amplitude. This can be extended to a distribution of number densities, arising from what can be thought of as a multi-domain sample. Essentially, the slight phase difference of the oscillations from each domain results in a smearing out of the sharp drops in magnetization. From (21), a (slightly more realistic) uniform distribution of number density $n_s \pm \Delta n_s$ will result in a width $\Delta B / B = \Delta n_s / n_s$ of the downward jumps of magnetization at the field B. The degree of inhomogeneity of actual samples is not necessarily easy to quantify; one might test if small samples give more ideal dHvA oscillations than larger ones taken from the same wafer (or measure their SdH and Hall number densities), but the scale of the inhomogeneity might be too small to detect with samples of usable size.

An arguably more realistic description of sample inhomogeneity is to assume that μ is constant throughout the 2DES, but that there are disorder induced lateral variations, as illustrated in figure 9, which cause n_s and hence the LLs to move up and down in energy across the sample. (Equivalently, the filling factor can be thought of as position dependent.) As a consequence, when averaged across the sample, the DOS of each LL has an associated mean value plus a broadening. A helpful interpretation of the broadened DOS produced by inhomogeneities is in terms of a 'phase smearing' or 'dephasing' concept: a position-dependent filling factor means that each portion of the sample contributes to the total oscillatory magnetic moment with a slightly different phase, thus reducing the oscillation amplitude. This qualitative argument of course says nothing about the precise form of the resultant DOS without further assumptions. However, it is
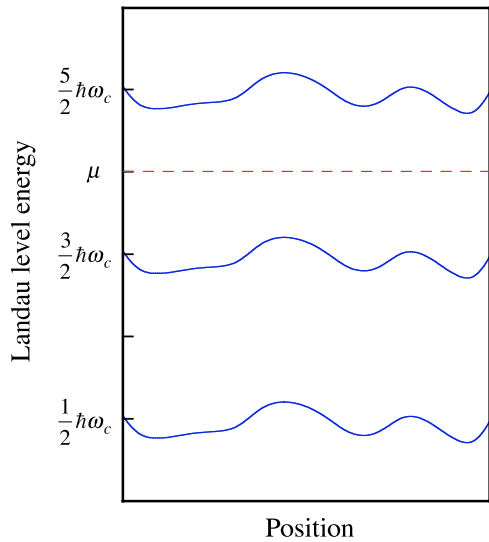
Figure 9. Schematic of the effect of disorder on the Landau levels (assumed spin-degenerate) of a 2DES. The energy of the levels varies randomly with position within the 2DES. The dashed red line is the electrochemical potential μ (assumed constant throughout the 2DES) corresponding to a filling factor $\nu = 4$. The position dependence of the levels results in the broadening of the density of states as discussed in the text.

interesting to note that although the dHvA effect will reflect the apparent DOS due to inhomogeneity, in contrast cyclotron resonance is expected to measure the *intrinsic* width of the LLs due to scattering alone [85]. This is because, if the scale of inhomogeneities is larger than the cyclotron radius, cyclotron resonance causes a spatially 'vertical' transition between LLs, which is the same, independent of position.

In fact, the scale of inhomogeneities is interesting in its own right. As mentioned above, we have effectively assumed that the characteristic length scale of any inhomogeneities is large compared with the classical cyclotron radius of the highest LL. In a series of papers [83, 84, 86–88] Watts showed a dephasing method to be an appropriate way to calculate the influence of any smoothly varying long-range scatterer on the dHvA effect amplitude. Watts argued that this will always (for 3D metals) result in a Dingle-type field dependence of the dHvA amplitude, which would equivalently be interpretable as a Lorentzian DOS, irrespective of the details of the inhomogeneities as long as they are statistically independent. (Furthermore, he suggested that conventional scattering can in fact be thought of as equivalent to dephasing.)

A similar interesting approach to this phase smearing concept has been put forward by Harrison and Singleton [89]. Although their model was specifically for the dHvA effect in inhomogeneous alloys, it could apply equally to a 2D system with inhomogeneous number density. They also find that under quite general assumptions of dopant atoms in a host material, the resultant statistical inhomogeneity leads naturally to an apparent Lorentzian broadening of the LLs without any electron scattering effects. Thus one can envisage that in a 2D system, the random distribution of dopant atoms can lead to the same behaviour. As a crude estimate of the importance of this effect, consider a modulation doping density of 4×10^{15} m^{-2}

with a spacer layer of 30 nm. If an electron consequently senses the potential of dopants in a circle of radius say 90 nm, i.e. about 100 dopant atoms, this would result in a statistical variation of about 10%.

Closely related to these simple models of inhomogeneity, other possible theoretical descriptions of the QHE, not invoking localized states, have been proposed by a number of authors. Woltjer [90–92] has investigated the effects of sample inhomogeneity of a few per cent, which leads to a position-dependent *local* filling factor and resistivity tensor $\rho(x, y) = \rho(\nu(x, y))$. The Hall resistance R_{xy}, expressed as an average of the Hall field and longitudinal current, mixes the transverse and longitudinal resistivity tensor components and was shown to lead to plateaux in R_{xy} which nevertheless remain accurately quantized. The influence of inhomogeneities in two-dimensional systems was also used [93] to provide an alternative explanation for the apparent large field-independent background DOS in magnetization and other experiments (capacitance, heat capacity), and again a few per cent variation in electron density was sufficient to explain observations.

2.2.2. Spin-splitting. The influence of electron spin was ignored in writing (2), which actually takes the form

$$\epsilon_\ell = \hbar\omega_c \left(\ell + \tfrac{1}{2}\right) \pm \tfrac{1}{2} g^* \mu_B B \qquad (27)$$

where g^* is the electron g-factor and $\mu_B = e\hbar/2m_0$ (with m_0 the bare electron mass) is the Bohr magneton. This means that the dHvA effect is in principle influenced by electron spin, but for it to be visible requires that the spin-splitting is comparable to or greater than Γ and $k_B T$ (and hence the oscillations have significant harmonic content). For a free electron g^* is almost exactly 2, and $\tfrac{1}{2} g^* \mu_B B$ is then exactly equal to $\hbar\omega_c$. Although $\hbar\omega_c$ is about 15 times larger in a GaAs-based 2DES, suggesting that the spin-splitting is comparatively small, the value of g^* depends on the parameters of the heterostructure, and is known to be field- and n_s-dependent due to exchange enhancement. For typical densities and high mobility the splitting becomes sufficiently enhanced to be observed in moderate fields, showing up in dHvA as additional jumps at *odd* filling factors (see for example figure 10).

For small LL broadening and low temperature, the jump Δm in magnetic moment *per electron* is roughly equal to the corresponding energy gap divided by the field B, so that the spin-splitting energy can be estimated. Using this method Zhu *et al* [71] for example found a g^* value of ~4.8 at about 7 T ($n_s = 4.9 \times 10^{15}$ m^{-2}, $\mu_H = 130$ m^2 V^{-1} s^{-1}) in one sample (which was bulk modulation doped), but only ~2 in a slightly poorer mobility δ-doped sample. (The measurements were after sample illumination which had the effect of suppressing otherwise dominant eddy currents.) These results are in stark contrast to those of Wiegers *et al* [73] on a δ-doped sample of similar characteristics ($n_s = 4 \times 10^{15}$ m^{-2}, $\mu_H = 100$ m^2 V^{-1} s^{-1}) where jumps at all the odd filling factors ν from 3 to 13 were reported, with similar strength to the even filling factors. Spin-split odd filling factors have also been reported by Schwarz *et al* [75] and they extracted a value of g^* of 5 from the dHvA jump at $\nu = 3$ occurring at
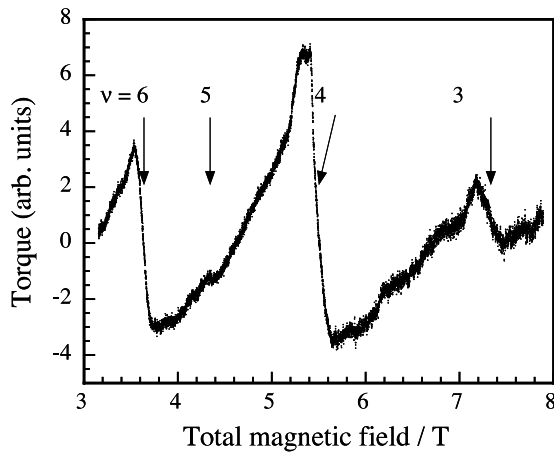
Figure 10. dHvA features at odd filling factors $\nu = 3$ and 5 in a 2DES with $n_s = 4.9 \times 10^{15}$ m^{-2} and $\mu_H = 130$ m^2 V^{-1} s^{-1} at a temperature of 540 mK. After Zhu *et al* [71].

about 6.5 T in their sample ($n_s = 4.75 \times 10^{15}$ m^{-2}, $\mu_H = 140$ m^2 V^{-1} s^{-1}). By examining the size of the odd filling factors over a wide range of field (in a very high-mobility sample, $\mu_H = 900$ m^2 V^{-1} s^{-1} with n_s around 3×10^{15} m^{-2}), Wilde *et al* [77] were able to extract the field dependence of g^*, which was found to vary from 7 at $\nu = 1$ to 3 at $\nu = 15$.

2.2.3. Constraints on number density. In interpreting dHvA data in a 2DES it is natural to assume that the number density n_s is a fixed quantity. However, this basic assumption has been questioned by a number of authors in the context of GaAs/(Al, Ga)As-based 2D systems, and has profound implications beyond just the dHvA effect. A number of authors have considered that quantum Hall plateaux can be caused by such an effect [78, 94].

A mechanism by which the number density might vary is if the 2DES can exchange carriers with another charge reservoir. Xu [78] made self-consistent Poisson–Schrödinger calculations of the electrostatics of single quantum wells. He found that, for samples with a thin enough spacer thickness and large enough modulation doping, Landau quantization will lead to oscillations in n_s (and hence oscillations in the confining potential) as charge is transferred between the 2D channel and dopant layer. The value of μ in the 2D channel can be thought of as 'pinned' to its value in the dopant layer, and the subband energy levels will oscillate with respect to it as charge flows in or out. Thus, the dopant layer acts as an electron reservoir in contact with the 2DES. An important consequence of this is that it leads to plateaux in the Hall resistance and will therefore contribute to the QHE. Similar results were found for one- or two-subband occupancy. Observations of oscillations in the recombination energy of electrons with photoexcited holes in a δ modulation-doped heterojunction [95] support this idea. Also, cyclotron resonance data [96, 79] strongly indicate oscillations in n_s, and have been found to agree well with n_s as calculated classically using the measured Hall effect in the same samples [79].

Interesting measurements were reported by Schaapman *et al* [97], who examined the dHvA effect in a GaAs/(Al,

Ga)As heterojunction containing two subbands. They found oscillations which were *not* periodic in inverse field and departed from the ideal sawtooth form, presenting triangular-shaped oscillations of reduced amplitude (around 0.5 μ_B^* per electron), which they explained using a magnetic-field-dependent self-consistent model of the electrostatics of the 2D system. The wavefunction of the second subband is particularly sensitive to changes in the potential. Further experimental and theoretical evidence to support the idea of a magnetic-field-dependent 2D electron density in a single subband comes from magnetophotoluminescence studies on modulation-doped asymmetric GaAs/(Al, Ga)As quantum wells [98]. Recently, the electron reservoir model has been proposed to explain features of magnetoplasmon dispersion in high-mobility 2D electron systems [99].

In summary then, there is growing evidence that oscillation in number density with magnetic field is a general feature of III–V semiconductor quantum wells and heterojunctions, and that they should be treated as open systems with a degree of coupling with some outside reservoir(s). A simple way of modelling this situation (see references [81, 56] for example) is to consider a 2DES in thermodynamic equilibrium with a reservoir having a constant DOS D_{res}. The total electron density N is constant and can be expressed as

$$n_s(\mu) + D_{res}\mu = N \qquad (28)$$

where μ is the common chemical potential. If D_{res} is zero, μ will oscillate as previously discussed in section 2.1.4 to maintain constant n_s, while if $D_{res} \to \infty$ then μ will be fixed. For finite D_{res} it is easy to show from (28) that the high-field side of the sawtooth oscillations of μ, which has infinite slope in the ideal case, now has a finite slope of approximately

$$\Delta\mu/\Delta B \approx g_L \nu / D_{res} B \qquad (29)$$

with g_L the LL degeneracy (3). The effect of two extremes of a pinned n_s or pinned μ on dHvA oscillations are nicely illustrated in figure 1 of Harrison *et al* [56]. (In this case the charge reservoir is provided by another portion of the Fermi surface of a quasi-two-dimensional metal.) We should note here that the DOS model (26) treated earlier does *not* assume contact with a separate reservoir (all the electrons comprise a single 2D subband), but it will have a similar effect to a partial pinning of μ produced by a small value of D_{res}.

2.2.4. Multi-subband samples. Alexandrov and Bratkovsky [100–102] reported the interesting fact that, in a 2DES with more than one occupied subband, the requirement of a constant total number density would lead to extra frequency components in the dHvA effect. In the 3D case, different extremal orbits of the Fermi surface each contribute additively to the total dHvA signal, but in 2D the oscillations due to each subband are effectively coupled together by the requirement of fixed *total* n_s. The reason for this is that oscillations in μ required to keep constant *total* number density must necessarily result in oscillations in the occupancy of the individual subbands. (A clear illustration of this fact in the context of SdH oscillations was given by Portal *et al*

[103].) This nonlinear coupling thus results in sum and difference combination frequencies of both the fundamental and the harmonic components of the Fourier spectrum of the oscillations. Shepherd *et al* presented dHvA evidence for this effect [80] in a three-subband InGaAs quantum well. (Weak combination frequencies were also found in SdH data taken on a Hall bar fabricated from the same material, indicating that contacts to the 2DES did not result in complete pinning of μ in the well.) The theory of the effect was studied in some detail by Champel [37] who also examined the influence of an electron reservoir as described in section 2.2.3 and derived an analytic formula to describe the dHvA harmonic components. Despite some disagreement in the literature as to the derivation of analytic formulae [104–106], the essential physics behind the effect remains clear.

As for the single-subband case, it is by no means certain that the total number density is constant in a multi-subband sample and Champel's results [37] are useful here. As also discussed in section 2.2.3, experimental investigations by Schaapman *et al* [97] of dHvA in a two-subband sample found evidence that n_s oscillated with field, and this possibility had been discussed previously by Shepherd *et al*. Only in the extreme limit of fixed μ (with respect to the subband energies) would the dHvA oscillations from each subband be decoupled, and single dHvA frequencies from each subband be observed. Thus a systematic study of multi-subband samples can reveal the degree to which μ is pinned in a real 2DES.

2.2.5. Equilibrium magnetization measurements of the fractional quantum Hall effect.

For a review of the fractional quantum Hall effect (FQHE), see Chakraborty and Pietiläinen [107]. The phenomenology of the FQHE is the same as that of the integer QHE: mobility gaps in the DOS lead to minima in ρ_{xx} accompanied by plateaux in ρ_{xy}. However the origin of the mobility gaps is different: in the case of the integer QHE it is LL quantization, but in the case of the FQHE it is the electron–electron interaction. Consequently, FQHE energy gaps are at least ten times smaller, and observation of the equilibrium magnetization oscillations associated with the effect represents a significant experimental challenge. Calculations of the energy gap, Δ, give $\Delta = Ke^2/4\pi\epsilon l_B$ ($l_B = (\hbar/eB)^{1/2}$ the magnetic length) with $K \approx 0.1$ for $\nu = 1/3$ and $2/3$ [108].

There has been one report of a measurement of the equilibrium magnetization of the FQHE [3]. The authors gate-modulated the number density of a high-mobility 2DES ($n_s = 0.97 \times 10^{15}$ m^{-2}, $\mu_H = 800$ m^2 V^{-1} s^{-1} at 0.3 K), and measured $\partial M/\partial n_s$ using a superconducting pick-up loop surrounding the 2DES, connected to a low-noise SQUID. By sweeping the gate voltage at fixed magnetic field they were able to reach LL filling factors below 1/3, at magnetic fields up to 10 T. In addition to oscillations at odd and even integer filling factors, features were also observed at $\nu = 1/3, 2/3, 4/5, 4/3, 8/5$ and $5/3$. They found good quantitative agreement in the size of the magnetization jump at $\nu = 1/3$ compared with calculations of Δ [108].

It has since been established [4] that changing the number density of a 2DES by sweeping a gate induces non-equilibrium
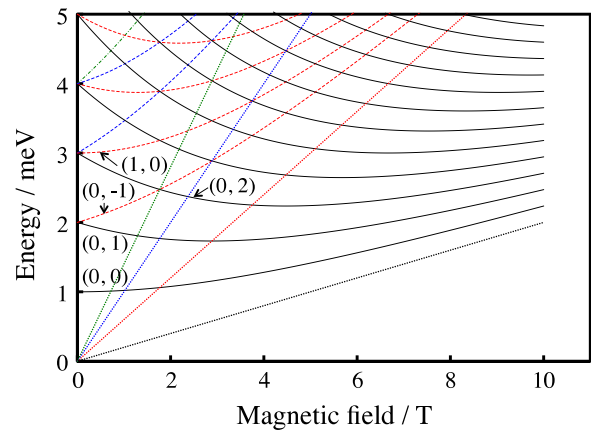
Figure 11. The Fock–Darwin spectrum of a quantum dot with parabolic confinement, subjected to a magnetic field. The characteristic energy of the dot is 1 meV and $\hbar\omega_c$ is 0.4 meV T^{-1}. Some of the levels are marked with their quantum numbers (ℓ, m). At high magnetic fields, levels denoted by solid black lines converge on the lowest LL (black dotted line); red long-dashed lines converge on the first excited LL (red dotted line); blue short-dashed lines converge on the second excited LL (blue dotted line).

circulating currents (the subject of section 3 of this review) which swamp the dHvA signal. It would seem possible that these might be responsible for some of the FQHE features observed.

2.2.6. Magnetization measurements of quantum dots and quantum wires.

The energy spectrum for electrons confined within a 2D parabolic potential, forming a quantum dot, with a magnetic field applied perpendicular to the lateral confinement directions, is the Fock–Darwin spectrum [109, 110]:

$$E_{\ell m} = (2\ell + |m| + 1)\hbar\left[\omega_0^2 + \frac{1}{4}\omega_c^2\right]^{1/2} - \frac{m}{2}\hbar\omega_c, \quad (30)$$

where $\ell = 0, 1, 2, \ldots, m = 0, \pm 1, \pm 2, \ldots$, and $\hbar\omega_0$ is the characteristic energy associated with the parabolic confinement. This spectrum is shown in figure 11. At zero magnetic field the energy levels are those of the confining potential, each level including states with the combinations of ℓ and m such that $j = 2\ell + |m|$ is the quantum number defining the level energy, $E_j = j\hbar\omega_0$. Combinations of ℓ and m for a few of the levels are shown in the figure. When the magnetic field is applied the degeneracy of these levels is lifted and the states with different values of ℓ and m follow different trajectories, until, in the limit of high magnetic field, when the magnetic length becomes much smaller than the confinement length of the quantum dot, the spectrum tends to the 2D case of equally spaced LLs (the dashed lines in the figure). The equilibrium magnetization of a quantum dot with parabolic confinement has been calculated for non-interacting electrons [111] and including interactions [112]. dHvA-like oscillations occur consisting of upward pointing cusps and shallow minima (see for instance figure 2 of [111]), the cusps occurring when all the levels tending towards a given LL become depopulated. The oscillation amplitude

(in effective Bohr magnetons per electron) is substantially smaller than in the 2D case. Superimposed upon this are high frequency Aharonov–Bohm-like oscillations. Schwarz *et al* [75] measured the magnetization of an array of 10^6 quantum dots of average diameter 550 nm, estimated to contain $\sim$230 electrons per dot, and compared it with that of the unprocessed 2DES. The dots were integrated into a GaAs cantilever magnetometer (see section 1.2). The 2DES showed the expected sawtooth dHvA oscillations, approaching the ideal amplitude of ± 1 effective Bohr magneton per electron. In contrast, the quantum dots showed only two weak oscillations, which were much more sensitive to temperature than the 2DES dHvA. They identified these features as occurring when the $\nu = 2$ and 4 LLs of the quantum dots depopulate, though the $\nu = 4$ feature was at an unexpectedly low magnetic field.

There has also been one report of magnetization measurements of quantum wires [113] and a theoretical study [114]. In the experiments, the magnetization oscillations resembled those of a 2DES with reduced mobility and reduced density compared with the host material; the oscillations did not correlate well with the model calculations. These are areas that clearly need further investigation.

3. Non-equilibrium induced currents

In 1980 von Klitzing *et al* [115] reported the discovery of the quantum Hall effect: that the Hall e.m.f. in a 2DES shows plateaux centred around integer values of the filling factor ν. Crucially, the corresponding Hall resistance (i.e. transverse magnetoresistance) at these plateaux takes the quantized values $h/\nu e^2$. In such measurements, a longitudinal current flows along a bar of 2DES material through contacts at either end, and the (transverse) Hall e.m.f. is measured using contacts at either side of the bar. In this section we describe how the quantum Hall effect can be measured using magnetometry, through the detection of circulating currents which are induced in a ring, disc, or (more commonly) square-shaped 2DES by a time-varying perpendicular magnetic field.

A schematic representation of the experiment is shown in figure 12 in which a sweeping magnetic field produces an e.m.f. around the perimeter of the 2DES, resulting in a circulating current I whose associated magnetic moment IA (A the area, πR^2, of the 2DES) is detected by the magnetometer. (The real current distribution will differ in several respects from this simple picture, as discussed in section 3.4.) The current, flowing in a magnetic field, is subject to the Lorentz force which causes a build-up/depletion of charge towards the edge/centre of the disc. This results in a (non-uniform) radial Hall electric field E.

Although this experiment essentially measures the magnetoresistance, it has several unique features. First, it is contact free. In conventional QHE experiments on Hall bars, dissipative hot-spots are known to occur at the current contacts, while at low currents the QHE is dissipation free elsewhere [116, 117]. At higher currents, the breakdown of the non-dissipative QHE occurs first at these hot-spots and gradually permeates into the rest of the 2DES. Magnetization measurements therefore enable us to study transport in a
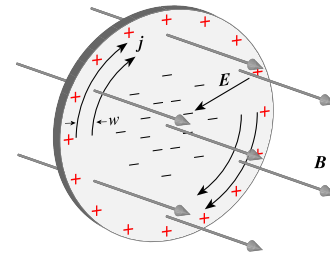

Figure 12. Highly schematic conception of induced eddy currents in a disc-shaped 2DES, radius R. A circulating current I flows around the sample perimeter. This current is assumed to flow over a characteristic width w so the magnitude of the current density is $j = I/w$. In the quantum Hall regime where $\sigma_{xx} \to 0$ the electric field E is virtually at right angles to the current flow, being the Hall field. The redistribution of charge shown corresponds to the case in which B and $\partial B/\partial t$ are parallel (an up-sweep).

virtually dissipation-free environment, and to investigate the intrinsic QHE breakdown avoiding the extraneous effects of contacts. Second, induced currents are excited by applying a *fixed* e.m.f. around the sample (produced by sweeping the magnetic field at a constant rate). In contrast, conventional measurements on Hall bars use *constant current* excitation. These two approaches yield fundamentally different results in systems in which dissipation increases with temperature (the QHE driven to high-current breakdown is such a system). Driving a constant current through the system can lead to thermal runaway [118, 119], but exciting the system with a constant e.m.f. does not (see equation (C.14)). Consequently induced currents can probe the breakdown regime more controllably. Third, the geometry of the 2DES in induced current measurements is unusual: it has one edge, in contrast to a Hall bar that has two, or a Corbino sample that has none.

Experiments are typically conducted at magnetic field sweep rates between 0.1 and 10 mT s^{-1} and at these sweep rates induced currents only become detectable under the conditions of the QHE—near integer (or some fractional) filling factors—and at temperatures sufficiently low for the quantum Hall plateau to be well quantized and the associated minimum in the magnetoresistance sufficiently deep. Typically this means below 1.5 K for the integer QHE and below 100 mK for the fractional QHE. An example is shown in figure 13. The induced currents are easily distinguished from dHvA oscillations because they reverse polarity when the magnetic field sweep direction is reversed. It is not common to see both dHvA and induced currents reported in the same experiment because induced currents rapidly increase in size as the temperature is reduced and overwhelm the dHvA signal. However, a few examples of both can be found in the literature, for example in figure 2 of Potts *et al* [51] and figures 2 and 3 of Schwarz *et al* [75].

It is also possible to induce currents by sweeping the 2DES number density at fixed magnetic field [4]. In these experiments a square 2DES with four ohmic contacts and a gate is placed on a magnetometer and the magnetization and electrical transport measured simultaneously. Induced currents, which reverse when the gate voltage sweep is reversed, are observed in the magnetization. The gate voltage
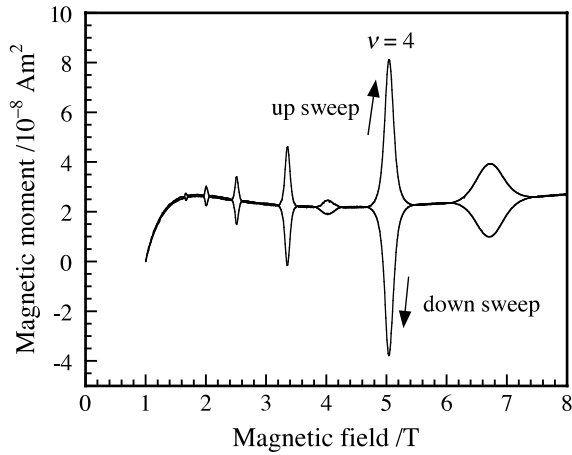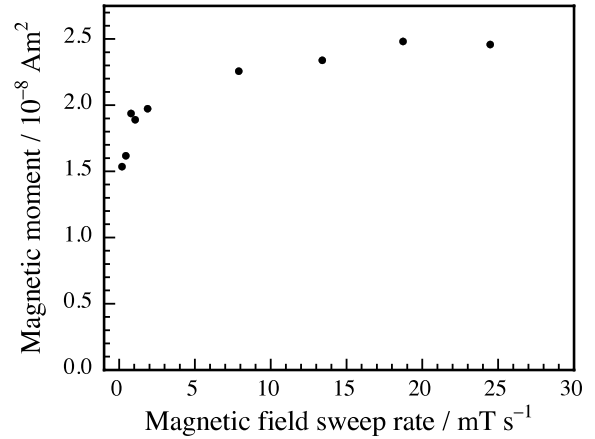
Figure 13. Magnetic moment versus magnetic field for a 2DES with $n_s = 4.4 \times 10^{15}$ m^{-2} and $\mu_H = 50$ m^2 V^{-1} s^{-1}, at $T = 50$ mK. Peaks at integer filling factors $\nu = 3, 4, 5, 6, 8, 10$ and 12, whose polarity reverses when the sweep direction is reversed, are caused by induced currents. In this sample, the much smaller equilibrium magnetization (dHvA) oscillations are completely masked by these non-equilibrium features.

causes electrons to flow into/out of the 2DES via the ohmic contacts. This flow is initially towards the centre of the sample, but the Lorentz force rapidly channels the currents entering the 2DES into tangential induced currents. The authors also observe a pronounced hysteresis in the shape of the magnetization versus filling factor, which they model in terms of the change in area of compressible and incompressible regions in the 2DES as a function of filling factor. A similar hysteresis is sometimes observed between different magnetic field sweep directions, the mechanism for which is discussed in section 3.4.2.

It is important to recall, as first noted in the context of the QHE by Macdonald *et al* [120], that unlike the 3D case the Hall electric field and the current density are necessarily highly non-uniform across a Hall bar and are accompanied by both edge charge and a redistribution of the charge density in the bulk. Similar considerations apply to the case of induced eddy currents, as discussed in section 3.4.1.

3.1. General I–V characteristic of induced currents

A typical plot of magnetic moment peak height (a measure of maximum current) versus magnetic field sweep rate (a measure of induced e.m.f.) is shown in figure 14. This plot, which can be thought of as an *I–V* characteristic, may be linear in samples of relatively low mobility and at temperatures above ~1 K (see section 3.1.1), but is highly nonlinear at low temperature, even down to the slowest sweep rates used (~1 × 10^{-4} T s^{-1}). The induced e.m.f. is incapable of increasing the magnetic moment above a saturation value m_s regardless of sweep rate. Only at elevated temperatures and in low-mobility 2DES does the apparently linear regime at low currents become accessible. The nonlinear behaviour has been interpreted in various ways, but is believed to be a manifestation of high-current breakdown of the QHE, discussed in more detail later.


Figure 14. Magnetic moment versus magnetic field sweep rate for the induced current at $\nu = 6$ in figure 13, equivalent to the *I–V* characteristic of the 2DES.

3.1.1. Simple model for the linear regime. In the simplest model [121] the azimuthal induced electric field E_ϕ at radius r due to the change of flux $\Phi(r)$ linking a circular sample produces a circulating current density $J_\phi = E_\phi/\rho_{xx}$. Integration yields a total induced moment in a circular sample of radius R

$$ m = \frac{\pi}{8} \frac{1}{\rho_{xx}} \frac{dB}{dt} R^4. \tag{31} $$

(The numerical prefactor is modified for a square or rectangular sample.) Measurement of the total magnetic moment m thus gives information about the resistivity of the 2DES [122]. Peaks in the eddy currents are therefore seen around both integer [123] and fractional [124] filling factors, where minima in ρ_{xx} occur. Equation (31) can form the basis for measuring the resistivity of the 'zero-resistance' QHE state—if the induced moment versus sweep rate is linear. Morris *et al* [121] examined induced currents at $\nu = 2$ and 1.25 K in a GaAs/(Al, Ga)As heterojunction 2DES ($n_s = 1.4 \times 10^{15}$ m^{-2} and $\mu_H = 30$ m^2 V^{-1} s^{-1} at 1.5 K) using a calibrated magnetometer. A linear relationship between the magnetic moments of the induced currents and the magnetic field sweep rate was seen (figure 15), as predicted by the model, except for a slight reduction at the largest sweep rates used (~5 mT s^{-1}). A value of ρ_{xx} of $(1.9 \pm 0.1) \times 10^{-4}$ Ω/□ was deduced. Furthermore, Morris was able to examine the R^4 size dependence predicted by (31) in some detail. In fact, discs and ring-shaped samples with inner radius R_1 and outer radius R_2 were examined, which would yield a magnetic moment scaling as $R_2^4 - R_1^4$ according to (31). A plot of the magnetic moments of the induced current peak at $\nu = 2$ versus the sample geometry term at a magnetic field sweep rate of ~2.36 mT s^{-1} was indeed found to be linear. From the line of best fit (effectively an average for all the samples examined) the value of the minimum in ρ_{xx} was calculated as $(1.9 \pm 0.3) \times 10^{-4}$ Ω/□ at 1.25 K.

The same procedure, although with different assumptions made about the distribution of current within the sample (an edge-weighted current distribution suggested by MacDonald *et al* [120]), and so with a different constant of proportionality, was used in early work by Eisenstein *et al* [8] for a 172-layer
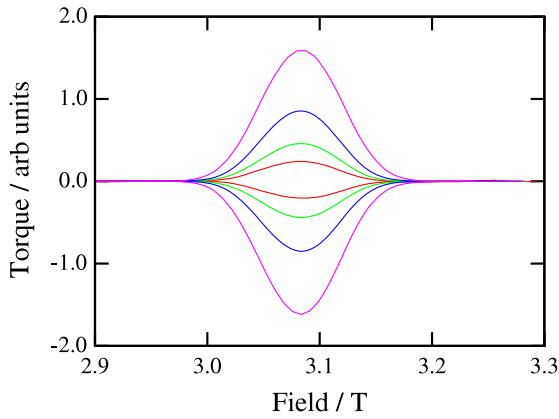
Figure 15. The $\nu = 2$ eddy current peak for a 2DES measured by Morris *et al* [121]. It shows linear increase of peak size with sweep rates of 5.91, 2.36, 1.18 and 0.59 mT s^{-1} (forward and reverse directions). A background slope on the magnetometer signal has been subtracted from the raw data, which have also been modified using a sweep-rate-dependent shift in magnetic field to allow for magnet time constant.
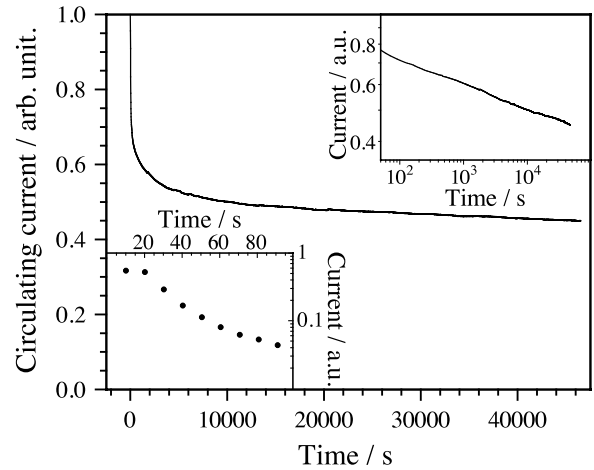
Figure 16. Decay of the induced current at $\nu = 2$ for a 2DES with $n_s = 1.7 \times 10^{15}$ m^{-2} and $\mu_H = 200$ m^2 V^{-1} s^{-1}, at $T = 88$ mK. The upper inset is a log–log plot of the decay from 100 s, demonstrating a power-law dependence. Having subtracted this power-law dependence from the data, the lower inset (a log–lin plot) shows an approximately exponential initial decay.

2DES at $\nu = 4$ ($n_s = 7.1 \times 10^{15}$ m^{-2} at $T = 0.23$ K). They found a resistivity of 10^{-6} $\Omega/\square$ at about 1.8 K. Measuring a resistivity this small in a conventional transport measurement would be a significant experimental challenge.

Morris *et al* [121] found (31) to be a good description of both the linear sweep rate and sample size dependence, but at lower temperatures, and in samples of better mobility, it no longer applies. Experimentally, it fails in two ways: first, the increase of m with sweep rate is no longer linear, but saturates—an effect which was attributed [123] to an eventual breakdown of the QHE, leading to an increase of ρ_{xx}. Second, if the sweep rate is abruptly stopped in the centre of an eddy current peak, the magnetic moment does not immediately drop to zero as implied by (31), but decays gradually with time. The nature of this decay has proved very informative as we will now discuss.

3.2. Lifetime of induced currents in the QHE

In early experiments the persistence of induced currents when the magnetic field sweep was stopped at integer ν was observed and single-exponential decays with time constants of 300 s (in a 172-layer 2DES, $n_s = 8.2 \times 10^{15}$ m^{-2}, $\nu = 4$ at $T = 0.4$ K) [7] up to 3.5 h (in a single-layer 2DES, $n_s = 3.6 \times 10^{15}$ m^{-2}, $\nu = 2$ at $T = 40$ mK) [122] were reported. The decay time τ was explained in terms of discharge of the (edge-weighted) Hall electric field, not included in deriving (31) which ignores the Lorentz force acting on the current. This force causes a build-up/depletion of charge at the centre/edge of the sample, and consequently supports the radial Hall electric field. Although not quoted by [122], including this effect (see appendix C) yields

$$\tau = Cw/\sigma_{xx}, \qquad (32)$$

where C is the capacitance per unit length of the edge and w is the effective width of the capacitor (the distance over which the

Hall voltage is mostly dropped). The energy stored inductively was found to be at least four orders of magnitude smaller than that stored in the capacitor and was therefore neglected [122]. Equation (32) suggests that another approach to measuring dissipation in the QHE, which does not rely on the linearity of the I–V curve, is to measure the decay of the induced current with time. From the decay times of the induced currents observed in these experiments, one can infer resistivities as low as 10^{-14} $\Omega/\square$ from (32).

The early experiments had significant limitations: Haavasoja *et al* [7] used a relatively low-mobility multilayer sample; and the decays of Jones *et al* [122] could only be tracked for a limited time because of instrumental drift. A more recent study using a more stable cryogenic system and low-drift electronics [12] was able to follow the decay in a high-mobility 2DES for over one day, with no significant drift [125]. The result (figure 16) was the observation of two distinct decay regimes: an initial fast decay (lower inset), possibly single exponential in form with time constant $\sim$30 s, followed by a much slower decay (upper inset), of power-law form, $I \propto t^{-n}$ (with n typically $\sim$0.07). This result implies that the resistivity is continually decreasing as the circulating current decreases. The authors inferred a resistivity of 4×10^{-15} $\Omega/\square$ after 12 h of decay. The picture suggested by these results is as follows. The initial e.m.f. provided by the sweeping magnetic field induces a current sufficiently large to cause breakdown of the QHE (see section 3.4), and the relatively large resistivity results in the initial fast decay. As discussed below, breakdown occurs when the Hall electric field exceeds a critical value; as the current decays, the Hall electric field eventually drops below this value, and the decay slows abruptly. One can then consider the current flowing in a single loop around the edge of the sample, having many possible relaxation paths (at impurities or edge imperfections where the Hall electric field is concentrated). As the current and the Hall electric field decay, the faster of these relaxation paths 'switch off' leaving

only the slower ones remaining. Eventually, in a finite sample, presumably only one decay path would remain and the decay would become exponential.

An alternative picture of the power-law decay is that the induced currents circulate around equipotentials in the disorder potential, forming many current loops of differing areas. Each loop will decay at a rate related to its capacitance and the resistivity. The faster decaying loops will disappear first, eventually leaving only one loop. Although both these models predict that the decay should eventually become single exponential (assuming that there is a finite cut-off for the longest possible time constant) it is important to emphasize that the experiment does not show single-exponential decay, even after the longest measurement period achieved, 24 h.

As a further alternative, one could consider a single current loop, decaying at a single 'weak point', through a quasi-elastic inter-LL scattering (QUILLS) process, as described in section 3.4. Then as the Hall electric field is reduced during the decay, the decay rate at this weak point is also reduced, resulting in a larger time constant and a sub-exponential (power-law) decay. In the case that the time constant at the weak point can be approximated as growing linearly with time ($t > 0$) as $\tau(t) \sim t/n$, so that the edge charge reduces with time as $\dot{Q} = -Qn/t$, then an exact power-law results, $Q(t) = Q(t_0)(t/t_0)^{-n}$.

Long-lived induced currents have also been detected in contacted 2DES [126, 127], and 2DES within electrostatically defined quantum-point-contacts and quantum dots [128, 129] (see section 3.3), and are presumably present, though undetected, in conventional transport measurements. Given that they are subject to a sub-exponential decay and are still half their original size after a day, it remains an intriguing open question how long they remain detectable before any departure from a power law is observed.

3.3. Electrostatic effects of induced currents

Currents induced around integer LL filling factors are accompanied by a transfer of charge due to the Lorentz force—the Hall effect. If we consider the disc-shaped 2DES of figure 12, then the tangential induced current causes a radial Hall electric field and hence a build-up of charge towards the perimeter of the disc. Specifically, when $\partial B / \partial t$ is parallel to B (an 'up-sweep') there is an accumulation of positive charge towards the perimeter of the disc and of negative charge towards the centre, while when $\partial B / \partial t$ is anti-parallel to B (a 'down-sweep') the reverse polarity occurs. This charge redistribution has been observed in single-electron transistor (SET) measurements of a 2DES [126, 127], and in conductance measurements of electrostatically defined quantum point contacts (QPCs) and quantum dots [128, 129]. The SET measurements probe the local electrostatic potential of the 2DES with sub-micron resolution. In addition to the zig-zag variation of the chemical potential, the SET also detected large induced current peaks at integer filling factors 3, 4, 5, 6 and 8. These reversed sign when the sweep direction was reversed and exhibited relaxation times up to some hours in high-mobility 2DES ($\mu_{\mathrm{H}} = 130$ m^2 V^{-1} s^{-1}). By comparing

the induced current peaks detected by several SETs at different positions, it was possible to infer that the induced current flows in a single loop around the perimeter of the 2DES, rather than in several smaller loops. Using a side gate to sweep the edge of the sample past the SET the authors demonstrated that the induced current flowed predominantly within a micron of the sample edge. In the measurements of QPCs, the QPC is formed by pinching off a 2DES with a split gate. In its pinched-off state conduction through the device occurs via tunnelling. Applying a sweeping magnetic field to the device so that the 2DES passes through integer LL filling factors results in hysteretic features in the QPC conductance, with the conductance being lower on an up-sweep than on a down-sweep. The authors compared the hysteretic features in these nanostructures with a direct measurement of the induced currents by magnetometry in an uncontacted 2DES from the same MBE wafer, and found clear correlation in the magnetic field, temperature and time dependences of the effects, strongly indicative of a common origin. The explanation for the hysteretic QPC magnetoconductance is that the accumulation of positive charge close to the QPC (i.e. at the edge of the 2DES on each side of the QPC) during an up-sweep increases the potential of the tunnelling barrier and hence reduces conduction through the barrier. The negative edge charge built up during a down-sweep has the opposite effect. In a separate experiment the authors also demonstrated a similar hysteretic effect in the Coulomb blockade of an electrostatically defined quantum dot.

3.4. Breakdown of the QHE

Breakdown of the QHE in 2DES continues to be an intensely researched area [130]. Very soon after the discovery of the QHE [115] it was recognized that the effect was subject to limitations: there is a gradual weakening (reduced plateau width and increased error in plateau quantization) upon increasing the temperature, and an abrupt weakening as a function of current [131]. The high-current breakdown is important both from fundamental and technological viewpoints. From a fundamental point of view, studies of breakdown give us an insight into the spatial distribution of current in the QHE, and understanding the mechanism for breakdown provides an explanation for why the QHE quantum fluid state is so robust. From a technological viewpoint, the breakdown regime is important in metrological applications because these involve measurement of the QHE at as high a current as possible, short of breakdown.

Breakdown occurs in Hall bars at integer filling factor ν when the current density exceeds a critical value (depending on the details of sample geometry and quality) and is characterized by a sharp increase in the longitudinal resistance ρ_{xx} away from its virtually dissipation-free value $\rho_{xx} \rightarrow 0$ observed at low temperature.

The current distribution is important in discussion of the breakdown of the QHE, because it is the maximum current *density* within the sample (or equivalently the maximum Hall electric field) that determines whether breakdown will occur. Many of the phenomena associated with the QHE are very

successfully described by a model in which current is carried by edge states, 1D channels corresponding to LL skipping orbits [132]. However, the edge state picture by itself does not describe the current distribution across a Hall bar. The Hall current arises from the drift velocity of electrons in crossed electric and magnetic fields (appendix B) and is carried by *all* electrons of the 2DES, not just those around an energy μ—a point emphasized by many authors (see [133] section IV, [134] chapter 4 and [135] for example)— and can be non-zero in the bulk.

Refinements of the edge state model taking into account electron–electron interactions predict that these channels become strips of compressible electron fluid alternating with regions of incompressible QH liquid [136], and scanning probe techniques have provided evidence for these strips [137]. However, Tsemekhman *et al* [135] have suggested that almost all of the *injected* current in the QHE regime flows through the bulk of the 2DES, an idea supported by the field-theoretical description of the QHE of Shizuya [138] which makes the distinction between chiral (diamagnetic) edge modes and bulk edge modes. In any case, in the high-current regime in which breakdown of the QHE occurs it is clear that edge state models are no longer appropriate; they would imply electron drift velocities many times larger than the sound velocity, at which energy loss due to spontaneous phonon emission would result in breakdown [130]. Instead, models in which currents flow in the bulk of the 2DES are more applicable. This does not however mean that the current distribution is uniform [120, 139].

The first observations of QHE breakdown [131] established that the sudden weakening of the QHE was caused by a sudden onset of dissipation: as the current passing through a Hall-bar sample was increased beyond a critical value, the longitudinal voltage along it would rise abruptly by several orders of magnitude. This nonlinearity in the I–V characteristic occurred at critical current densities, j_c, between 0.5 and 2 A m^{-1}. These reports also raised the issue of dissipation at the current contacts and its possible effect on critical current. These and other early experiments, carried out on Hall bars (widths 300–400 μm) [140, 141] or on Corbino-geometry samples [131, 142], were analysed assuming uniform current distribution, and therefore underestimated the critical current density.

Measurements of the dependence of critical current on Hall-bar width have gone some way to establishing the current distribution at breakdown. Balaban *et al* [139] observed a logarithmic dependence, which they explained in terms of the edge-weighted bulk current distribution proposed by MacDonald *et al* [120]. In contrast, Kawaji *et al* [143] observed a linear dependence. Meirav *et al* [144] resolved this apparent controversy by noting that different dependences of critical current on width are observed in samples having different levels of disorder: a logarithmic dependence is present in high-mobility 2DES, in accordance with the model of Macdonald *et al*; in low-mobility 2DES the currents follow a network of complicated percolating paths through the sample, dependent on the disorder potential and not accounted for within the Macdonald model, resulting in a more uniform
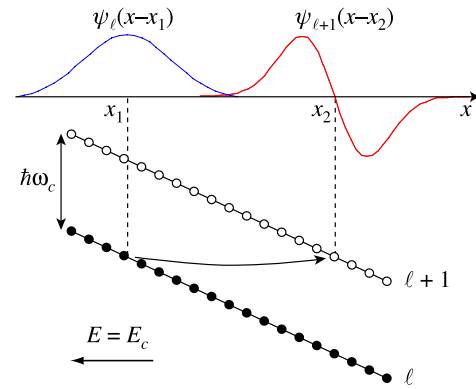
Figure 17. Schematic representation of quasi-elastic inter-Landau-level scattering, after Eaves *et al* [151]. The electric field E causes the LLs to acquire a slope eE, so that states in the lower occupied Landau level (ℓ) have the same energy as nearby states in the upper empty LL ($\ell + 1$) and can tunnel into them if perturbed by, for example, impurity or phonon scattering. The wavefunctions ψ_ℓ and $\psi_{\ell+1}$ overlap significantly when E exceeds a critical electric field E_c.

current distribution and hence a linear dependence of critical current on width.

Various mechanisms have been proposed for QHE breakdown, including an electron-heating instability [145, 146], intra-LL transitions involving acoustic phonons [147], formation of percolating metallic channels under the influence of the Hall electric field [148], and quasi-elastic inter-LL scattering (QUILLS) [149–151]. The first two of these models predict values of j_c in agreement with early experiments. The electron-instability model has also been used to explain a bistability in the breakdown [152], and the dependence of breakdown on Hall-bar length [118]. However, experiments assuming an edge-weighted current distribution, experiments on 2DES with short, narrow constrictions [153], and the magnetometry experiments discussed below, all give larger values of j_c, in better agreement with the QUILLS model. Since we will use this model to explain some of the magnetometry results, we now review its main predictions.

According to the QUILLS model, adjacent LLs, which are separated by an energy $\hbar\omega_c$ in the bulk of the 2DES, become tilted due to the Hall electric field. When this tilt becomes large enough to allow a significant overlap of the wavefunctions in the two levels (figure 17), scattering between levels can occur. Assuming the system is at integer filling factor ℓ (ignoring spin), then the ℓth LL is full and the ($\ell + 1$)th level is empty. Transitions from the ℓth to the ($\ell + 1$)th level therefore result in the onset of dissipation characterizing QHE breakdown. The onset is sudden because of the exponential dependence of the tunnelling rate on barrier width. From the figure, this occurs when the Hall field reaches a critical value E_c given by

$$E_c = \frac{\hbar\omega_c}{el_B[(2\ell + 1)^{1/2} + (2\ell + 3)^{1/2}]}, \qquad (33)$$

where l_B is the magnetic length. Momentum is conserved in such a transition either by emission of acoustic phonons, or by the recoil of impurities. The presence of an impurity may also

result in a local enhancement of the Hall electric field which itself would encourage breakdown.

It would seem that the model used to explain QHE breakdown depends on the specifics of the experiment, in particular the geometry and contact configuration of the Hall bar. This provides the motivation for studying breakdown in a contact-free geometry.

3.4.1. Magnetometry measurements of breakdown of the QHE. Nearly all QHE experiments are performed on Hall bars, although there are some measurements on Corbino geometries [154–157]. Corbino measurements are of interest since they avoid possible problems associated with contacts in Hall bars, but they are also geometrically very different from Hall bars in that edge states can play no role. In magnetometry experiments, we use a geometry which has essentially the simple circular symmetry of the Corbino geometry, but in which the current flows parallel to the edge as in a Hall bar. This geometry is closely related to Laughlin's well-known thought experiment [158]. Furthermore, there is *no electrical contact* to the sample. Thus investigations of induced currents detected via their magnetic moment offer a unique contact-free geometry in which to study breakdown of the QHE.

Following the early observation of the nonlinear *I–V* (magnetization versus sweep rate) characteristics of induced currents [9], the first breakdown investigations, on a 2DES with $n_s = 3.6 \times 10^{15}$ m^{-2}, mobility $\mu_H = 27$ m^2 V^{-1} s^{-1}, demonstrated the same abrupt increase in dissipation as the current is increased and used the saturation value of the magnetization to estimate j_c [123]. Assuming a uniform current distribution in this large (1 cm^2) sample yielded values of j_c lower than any previous experiments. However, using a more realistic edge-weighted current distribution as proposed by Balaban *et al* [139] (consistent with the relatively high mobility of the sample) yielded critical Hall electric fields near the sample edge consistent with the QUILLS model, but too high to be explained by other models.

In subsequent contact-free investigations of both the integer and the fractional QHEs (IQHE and FQHE) [124, 159], measurements of j_c as a function of filling factor were found to have a magnetic field dependence in good agreement with the piecewise $B^{3/2}$ behaviour predicted by the QUILLS model (33) for the IQHE. For FQHE breakdown, (33) should be modified by replacing $\hbar\omega_c$ with the energy gap, Δ, associated with the formation of quasiparticle–quasihole pairs (defined in section 2.2.5)—the parameter defining the robustness of the FQHE. Thus, a comparison of the FQHE critical currents with those for the IQHE provides a quantitative measure of Δ. The values obtained for $\nu = 1/3$ and 2/3 were found to be in good agreement with theory (for a review, see [107]), in contrast to previous measurements using conventional activated transport measurements. It is well known that activated transport measurements underestimate Δ because they are sensitive to the *global* energy separation between mobility edges. It was argued that QUILLS scattering occurs on length scales (of the order of l_B) which are much smaller than the scale of the fluctuations in the disorder potential and that breakdown was therefore a *local* process. The absolute values of
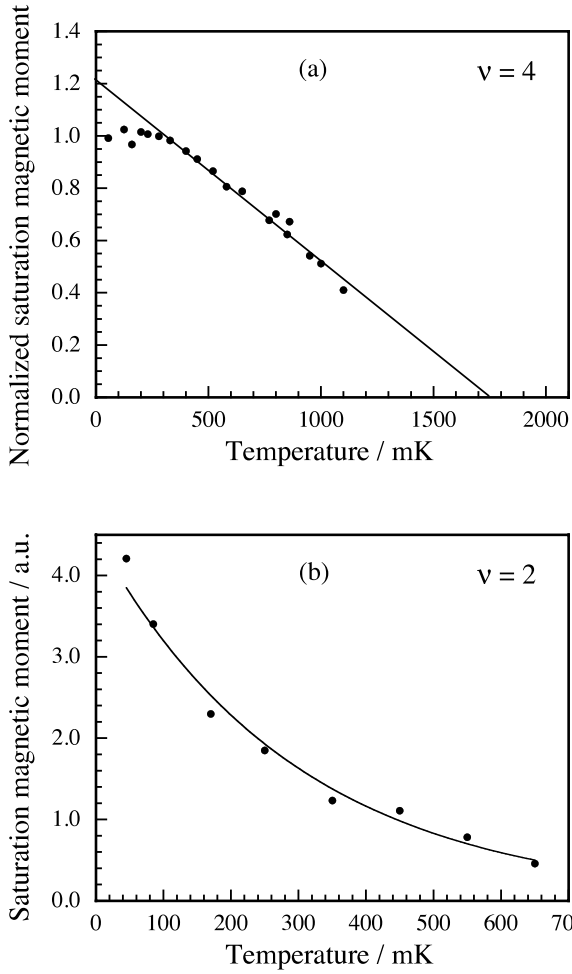
j_c (or equivalently E_c) reported in these investigations are even larger than predicted by QUILLS. Balaban *et al* [139] argued previously that larger than expected values of j_c could arise if the disorder potential split the 2DES up into domains. Assuming these domains took the form of strips along the direction of current flow, the total current through all strips would then be larger than the current through the sample treated as a single domain, because of the logarithmic dependence of current on width. It is important to note that quantitative agreement with the simple QUILLS model is not required in order to calculate Δ because Δ is obtained by *comparing* the FQHE induced currents with those of the IQHE. In an alternative analysis these results can be compared with the theory of composite fermions [160], in which the strongly interacting electrons couple to flux quanta to form (non- or weakly-interacting) composite fermions and the FQHE can then be considered to be the IQHE of these new quasiparticles. Δ is then a measure of the effective mass of composite fermions. The experiment yielded $m^*_{CF} = 0.32$ m_0 for both $\nu = 1/3$ and 2/3, somewhat smaller than the value obtained using conventional transport techniques [161].

In further magnetometry investigations, on both electron systems [162, 163] and hole systems [164, 165], it became apparent that there are a number of surprising aspects to breakdown in contact-free geometries. First, the saturation magnetic moment m_s (proportional to critical current) is higher in samples with lower mobilities. Second, the induced currents are only detectable at temperatures ~10 times lower than the cyclotron energy. Third, m_s itself has a temperature dependence (figure 18): in low-mobility samples ($\mu_H \lesssim 75$ m^2 V^{-1} s^{-1}), m_s falls linearly with increasing T, reaching zero at a temperature dependent on number density and filling factor, typically ~ 300 mK, and sometimes also plateaus at a maximum value at low temperature; in higher-mobility samples the drop off with temperature is faster, possibly exponential, and there is no observable low-temperature plateau.

3.4.2. Charge redistribution model. To explain the temperature dependence both of the induced currents themselves and of their saturation values at breakdown, a model based on the arguments of Dyakonov [166], modified to suit the unusual sample geometry, was invoked [163, 162]: if the sample is a disc of radius R the magnetic moment due to a tangential circulating current $j_\phi(r)$ is

$$m = \pi \int_0^R j_\phi(r) r^2 \, \mathrm{d}r = \pi \int_0^R \sigma_{xy} E_r(r) r^2 \, \mathrm{d}r \qquad (34)$$

where we have used the fact that in the QHE the Hall angle is 90° and hence $j_\phi = \sigma_{xy} E_r$, and E_r is the radial Hall electric field. E_r is created by the redistribution of charge under the influence of the Lorentz force. (In this discussion the microscopic details of current paths through the sample are ignored—we assume average current densities.) Dyakonov pointed out that in two-dimensional systems, charges could not accumulate solely at the edges but must be distributed over the disc. The extra electron density Δn in some regions
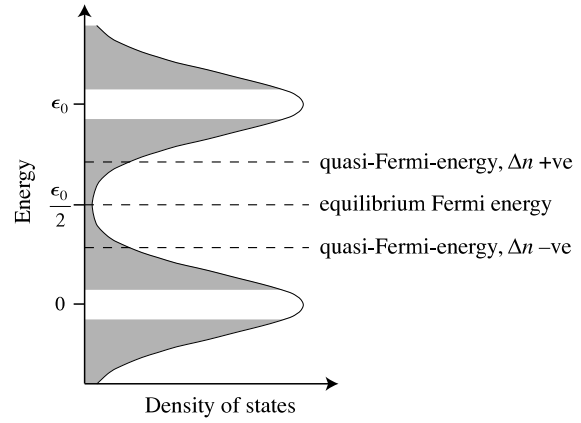
Figure 19. Two disorder-broadened LLs showing the position of the Fermi energy at integer ν. When the magnetic field is swept, electrons accumulate in or deplete from different regions within the 2DES. In regions of accumulation ($\Delta n +$ ve) the quasi-Fermi-energy increases; in regions of depletion ($\Delta n -$ ve) it decreases. This results in more thermally activated conduction. The shaded and unshaded regions represent the localized and extended states, respectively.

Figure 18. The temperature dependence of the saturation magnetic moment: (a) for the low-mobility sample of figure 13, m_s rises as the temperature is reduced, eventually reaching a plateau at low temperature. The saturation magnetic moment has been normalized to its low-temperature value. Above 1.1 K the I–V curve no longer shows a distinct saturation. (b) In higher-mobility samples there is an approximately exponential dependence. In this case, $n_s = 1.02 \times 10^{15}$ m^{-2} and $\mu_H = 100$ m^2 V^{-1} s^{-1}. The exponential fit, $m = m_0 \exp -T/T_0$, gives $T_0 = 297$ mK. The charge redistribution model (section 3.4.2) provides an explanation for these observations.

of the sample will raise the quasi-Fermi-energy (chemical potential) above its equilibrium position midway between LLs, and hence increase the probability of thermal activation of electrons from the highest full LL to the lowest empty one (figure 19). Conversely, in regions in which the electron density is depleted by Δn, the probability of thermal excitation of holes is increased. Thus the total probability of thermal excitation, and hence the dissipation is proportional to

$$\exp[-(\epsilon_0/2 - \Delta\mu(\Delta n))/k_B T]$$
$$+ \exp[-(\epsilon_0/2 + \Delta\mu(\Delta n))/k_B T]. \qquad (35)$$

The exponential dependence on $|\Delta n|$ accounts for the abruptness of QHE breakdown. To determine the temperature dependence of the effect, we assume that breakdown occurs at some threshold value of (35). At breakdown one of

the exponentials in (35) dominates and we can write the breakdown condition:

$$\exp[-(\epsilon_0/2 - \Delta\mu(\Delta n))/k_B T] = C, \qquad (36)$$

in which C is a constant very much less than unity. This provides an expression for $\Delta\mu(\Delta n)$ from which the critical value of Δn required for breakdown can be calculated:

$$\Delta n_c = \int_{\epsilon_0/2}^{\epsilon_0/2 + \Delta\mu} \rho(\epsilon)\, d\epsilon = \int_{\epsilon_0/2}^{\epsilon_0/2 + k_B T \ln C} \rho(\epsilon)\, d\epsilon. \qquad (37)$$

where $\rho(\epsilon)$ is the DOS of electrons.

To obtain the magnetic moment we next need to consider the electrostatic consequences of this departure from a uniform charge distribution. The Hall electric field depends on the distribution of excess charge $\Delta n(r)$. A reasonable first approximation for this distribution, which gives the maximum possible value of m in (34) while maintaining charge neutrality, is that there is a uniform *excess* charge $+e\Delta n_c$ for $r < R/\sqrt{2}$ and a uniform charge *depletion* $-e\Delta n_c$ for $R/\sqrt{2} \leqslant r \leqslant R$, the sign of the charges being reversed for the opposite sweep direction (inset to figure 20). Figure 20 shows the resulting Hall electric field, after a correction has been made for the unphysical sign reversal of the field close to the edge of the sample. Using this electric field distribution, the saturation value of the magnetic moment, m_s, can be calculated from (34):

$$m_s = \Lambda\pi\sigma_{xy}e\Delta n_c(T)R^3. \qquad (38)$$

Here Λ is a dimensionless constant which is $\sim$1.1 for the electric field distribution discussed above. Regardless of the exact distribution chosen, the conclusion is that m_s has the same temperature dependence as Δn_c, which we now discuss.

From (37) we see that the temperature dependence of Δn_c depends on the form of $\rho(\epsilon)$ in the localized-state region between the highest occupied and the lowest unoccupied LLs.
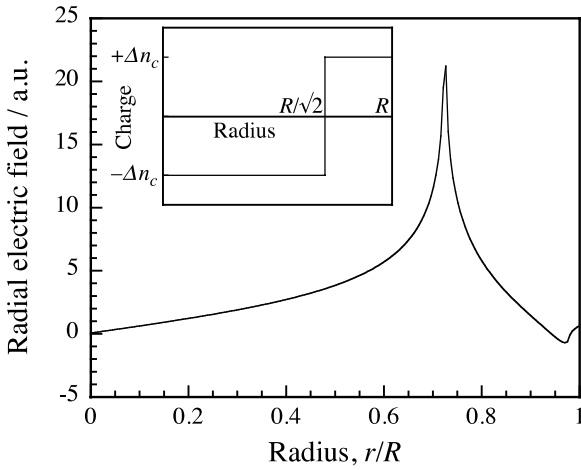
Figure 20. Radial electric field resulting from the charge redistribution model assuming a circular 2DES of radius R. Inset shows the assumed bipolar charge distribution, which would be caused by an up-sweep. The polarity of the distribution reverses for a down-sweep.

Figure 21. Induced currents in a 2DES with $n_s = 3.1 \times 10^{15}$ m^{-2} and $\mu_H = 78$ m^2 V^{-1} s^{-1}, at $T = 50$ mK. The charge redistribution model explains the asymmetry between up- and down-sweeps in terms of the different regions of excess charge and charge depletion shown in the insets, as discussed in the text.

Assuming that both of these LLs have the same shape, $\rho(\epsilon)$ will be constant in the immediate vicinity of $\epsilon_0/2$. For high-mobility 2DES, $\rho(\epsilon)$ will be very small at this point, but will quickly become substantially larger (exponentially larger if the LLs are Gaussian in shape) as we move away from $\epsilon_0/2$. From (37) the range of the integral decreases as T increases (note that ln C is negative) and so for high-mobility 2DES we expect a sharp (possibly exponential) reduction in Δn_c, and hence in m_s, with temperature. This is in agreement with the observations [162] of figure 18(b). In lower-mobility 2DES, the DOS is larger around $\epsilon_0/2$, and there might also be a constant background DOS in this region [167] as discussed in section 2.2. Because of the relatively large DOS, a larger charge build-up will be required to shift the quasi-Fermi-energy to its critical position, resulting in a larger value of m_s. Assuming that the DOS is a constant, ρ_0, over the range of integration, m_s becomes:

$$m_s = \Lambda \pi \sigma_{xy} e R^3 (\epsilon_0/2 + k_B T \ln C) \rho_0. \tag{39}$$

The linear decrease of m_s with T is in agreement with measurements (figure 18(a)), though a saturation of m_s at low T is also observed, suggesting that at the lowest temperatures QUILLS breakdown is occurring. Equation (39) predicts a link between the cut-off of m_s at high temperature and the LL energy separation, which enables these measurements to be used to determine the electronic g-factor [162].

This model also helps to explain the behaviour of the induced currents as a function of ν, near integer ν. The observation (figure 21) is that m generally decreases as the system moves away from exact integer ν, and that in some high-mobility samples there is a pronounced asymmetry between up-and down-sweeps [168]. Away from integer ν, μ lies closer to one LL than the other. For instance at $\nu >$ integer, μ moves towards the upper LL. In this case the shift in the quasi-Fermi-energy required for breakdown is less than at exact integer ν in regions with an excess of electrons, but more
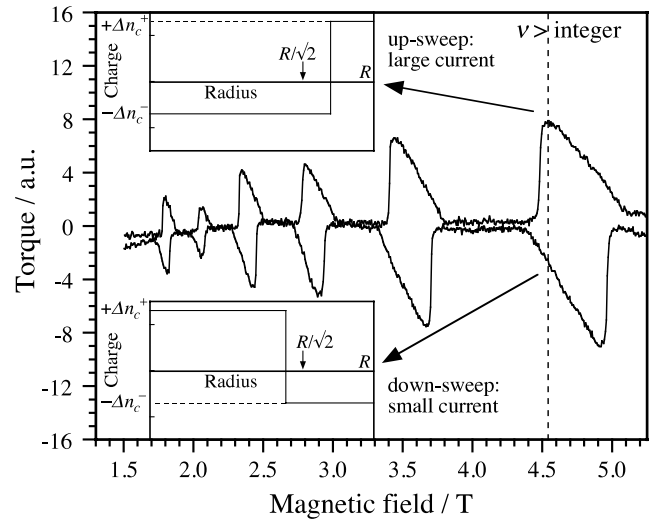
in regions with an electron depletion. As a result, breakdown requires the positive space charge regions to have larger charge density than the negative ones, Δn_c is larger for holes than for electrons, or $\Delta n_c^- < \Delta n_c^+$. As discussed by Matthews *et al* [168], this will cause an asymmetry between up-and down-sweeps: the condition of overall charge neutrality causes the boundary between the positive and negative regions shown in the inset to figure 20 to move away from $r = R/\sqrt{2}$, in a direction depending on both ν and the sweep direction. The sweep direction for which this radius is increased (reduced) will exhibit a larger (smaller) m simply because the area of the current loop has increased (decreased). For instance, if $\nu >$ integer then the boundary becomes larger than $r = R/\sqrt{2}$ for an up-sweep (upper inset in figure 21) and smaller than $r = R/\sqrt{2}$ for a down-sweep (lower inset). This mechanism may also explain the hysteresis seen in the swept-gate experiments of Faulhaber *et al* [4].

3.4.3. QHE breakdown as an example of self-organized criticality. A detailed examination of induced eddy current peaks, in samples of moderate mobility, revealed an unusual 'noisy' structure which seems to be a manifestation of QHE breakdown [169, 170]. This structure, not observed in early experiments [122, 123], was detected by improving the response time of the magnetometer measurements (using lock-in time constants 50 ms or less), rapid data acquisition, and slow magnetic field sweep rates. An example of the structure observed, from the data of Elliott *et al* [170], is shown in figure 22 for an approximately 10 mm square sample with $n_s = 3.5 \times 10^{15}$ m^{-2} and $\mu_H = 27$ m^2 V^{-1} s^{-1} at 4.2 K.

Noisy structure associated with QHE breakdown has been reported on several occasions [140, 171–173]. In particular, Cage *et al* [140] observed time-dependent fluctuations in longitudinal voltage drop in a current-carrying Hall bar near breakdown. However, the QHE breakdown observed in
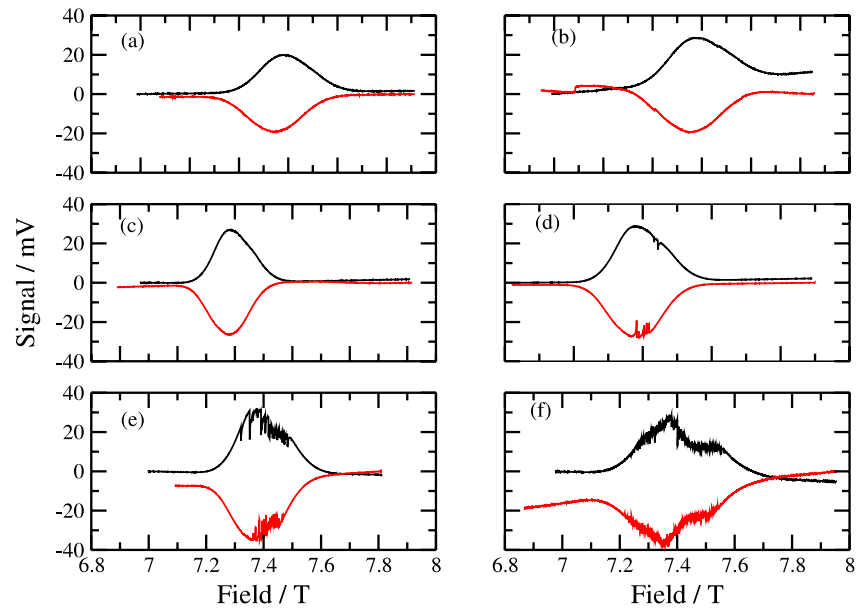
Figure 22. Temperature development of noise structure at the $\nu = 2$ eddy current peak. The magnetometer output upon sweeping the magnetic field up (upper curve) and down (lower curve) at 1.65 mT s^{-1} in sample NU762 develops structure below about 1 K. Temperatures in (a)–(f) are 1.58, 1.33, 1.21, 1.10, 0.95, and 0.58 K.

induced current experiments is different from those in Hall-bar experiments. In Hall bars the applied longitudinal current I_x is the controlled parameter, and the longitudinal voltage drop is a measure of ρ_{xx}. Once breakdown begins, independent of the microscopic mechanism involved, an increase in ρ_{xx} with constant I_x leads to an increased dissipation and a positive feedback which further increases ρ_{xx}. In contrast, in induced current experiments it is the induced electric field which is the controlled parameter (depending on the sweep rate) and an increase in ρ_{xx} now leads to a *decrease* in dissipation and a self-limited current (see equation (C.14)).

An interesting feature of the noise structure in figure 22 is that although it is not exactly reproducible, it always consists of a sudden decrease in the signal, followed by more gradual recovery towards the original size, irrespective of the field sweep direction. (Upon reversing the field sweep direction, the direction of all the features reverses, still with a sudden *decrease* in the signal size towards zero, followed by gradual rise towards the original size.) This recovery, illustrated in figure 3 of the paper by Phillips *et al* [169], is closely linear at lower temperatures but increasingly curved as the temperature is raised. The sizes and number of jumps were found to increase at low temperature.

Sometimes the noise jumps take a fairly regular form (although again not exactly reproducible) as illustrated in figure 23, which shows the same sample ($n_s = 4.8 \times 10^{15}$ m^{-2} and $\mu_H = 50$ m^2 V^{-1} s^{-1} at 4.2 K) as examined by Phillips *et al* [169]. An explanation for the recovery portion of the jumps was made by Elliott *et al* [170]: for any sample geometry, in the limit $\rho_{xx} \rightarrow 0$ around a Hall plateau, the current density j and electric field in the sample are essentially perpendicular. In figure 12 for instance the tangential circulating eddy currents (opposing the *change* of magnetic field) are perpendicular to the radial (Hall) field. The
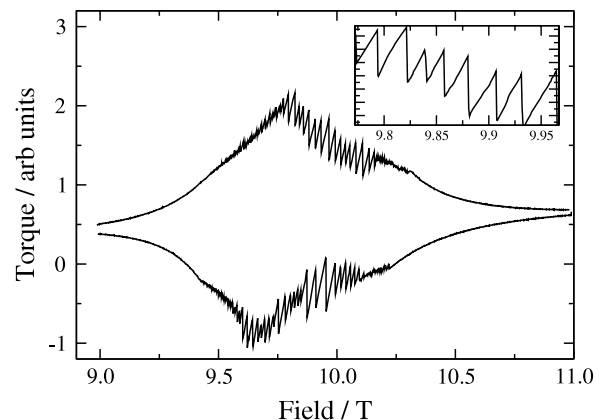
Figure 23. Noise structure at 68 mK of the $\nu = 2$ eddy current peaks (up- and down-sweeps) in sample T73. The inset is a zoom-in on a portion of the upper curve.

Hall voltage will therefore be dropped across the width w near the edge of the 2DES. If B is static, the eddy currents are almost constant, as noted above [122]. If B is swept, each additional flux quantum $\Phi_0 = h/e$ linking the sample radius R will transfer a charge $Q_0 = (ie^2/h)\Phi_0$ across w (where i is the plateau index) increasing both the Hall field and circulating eddy current *linearly* with magnetic field. The linear portion of the signal in figure 23 can thus be understood in terms of this model, and is fully consistent with the Laughlin thought experiment [158]. The interpretation of the structure observed in figures 22 and figure 23 is thus that as the magnetic field is swept, more charge is transferred until the critical Hall field is reached, at which point breakdown causes charge to be suddenly re-distributed across w. Once the discharge has reduced the Hall field sufficiently, the sweeping magnetic field

will tend to build up charge again until the process is repeated. This model was extended [170] to explain the curvature seen in the recovery at raised temperature; essentially, the slow increase of signal is governed by the same capacitor–resistor time constant $\tau = Cw/\sigma_{xx}$ (see equation (32) of section 3.2), as derived in (C.5), where C is the capacitance per unit length perpendicular to the width over which the Hall field is dropped.

In some samples (depending on their history of cool-down from room temperature to cryogenic temperatures) it appears that just a few weak spots for breakdown exist, and a fairly regular pattern results, whilst in others a much more complex pattern occurs. For the latter case, analysis of several samples suggested that the Hall field at breakdown is at a point of self-organized criticality (SOC). (This concept was introduced [174] to explain the ubiquity of $1/f$ noise and has since been applied to a wide range of physical phenomena.) Not only does the noise possess the general features observed in avalanche models of SOC, such as of magnetospheric activity [175] and of sandpiles [176], but there are compelling physical reasons for expecting a *self-organized* criticality. In particular, when a critical Hall field is reached, one would expect that breakdown causes charge to be re-distributed to the bulk in the form of an 'avalanche'. Once the avalanche has caused a discharge, the sweeping magnetic field will tend to build up charge again until the process is repeated. This is similar to the simple generic 'sandpile' model [174] of SOC. Thermal cycling and cool-down rates might be expected to affect any imperfections in the sample at which breakdown may occur. Most compelling, analysis of the size and frequency of the jumps produced a reasonable power law consistent with the predictions of SOC [177].

To understand fully the detailed mechanism of the noise jumps and their statistics, a microscopic model of the current distribution is required. One possibility is that the complex structure of the jumps is related to the picture discussed by Tsemekhman *et al* [178, 179] of a random resistor–capacitor network, originating from an inhomogeneous 2DES of interpenetrating compressible and incompressible regions throughout the bulk of the sample, where charge can transfer between isolated metallic (compressible) regions in the bulk via hopping. Irrespective of the precise cause of the breakdown, it appears likely that microscopically inhomogeneous current density plays a role. Scanning probe studies of quantum Hall breakdown while sweeping the magnetic field would be very informative in this regard.

4. Conclusions

Low-dimensional systems of electrons and holes in high magnetic fields at low temperatures show a wealth of exciting phenomena which have resulted in intensive investigations using conventional measurement techniques such as electronic transport and optics. The relatively novel technique of magnetometry provides fundamental information not obtainable using conventional probes. Equilibrium magnetization provides a probe of the equilibrium thermodynamics of the system and investigations have provided information about the shape of the LL DOS and its evolution with magnetic field. There remains controversy in this area however, and the intriguing prospect that the assumption of a fixed 2DES number density, independent of field, which underpins our understanding of the QHE, may be incorrect. Evidently, further theoretical and experimental work in this area is required. Non-equilibrium magnetization provides a contact-free electrical transport measurement which is suited to probing the regime of vanishing ρ_{xx} associated with the QHE which is inaccessible to conventional transport methods. The circulating induced currents responsible for the non-equilibrium magnetization can be extremely long-lived, persisting for as long as experiments have been able to track them (longer than one day). Their non-linear dependence on magnetic field sweep rate has provided new insights into the breakdown of the QHE by high currents. The recent observation that induced currents can influence the behaviour of electrostatically defined nanostructures offers the possibility of novel devices using induced currents to control electrical transport through such structures, which may have uses in quantum information processing. Developments in magnetometer design, using the beneficial scaling of cantilever sensitivity with reduced size, combined with novel detection schemes, offer the exciting prospect of studying nanomaterials such as carbon nanotubes and quantum dots.

Appendix A. Free electron in 2D in a magnetic field

Consider an electron of mass m^* and charge $-e$ in the presence of a field $\boldsymbol{B} = (0, 0, B)$ chosen in the z-direction, and in a potential $V(z)$, which represents the confining potential of an electron at a heterojunction or in a quantum well. The Hamiltonian is

$$H = \frac{1}{2m^*}(\boldsymbol{p} + e\boldsymbol{A})^2 + V(z) \tag{A.1}$$

where $\boldsymbol{A}$ is the vector potential with $\boldsymbol{B} = \nabla \times \boldsymbol{A}$. The energy eigenvalues can be deduced [180, 181] from the commutation relations for $\boldsymbol{\pi} = \boldsymbol{p} + e\boldsymbol{A}$ but here we move immediately to a real-space representation of the Schrödinger equation, requiring a choice of gauge for $\boldsymbol{A}$. The gauge chosen also affects the wavefunctions.

Various choices of gauge for A are possible; for example:

$$A = (-By, 0, 0), \qquad A = (0, Bx, 0),$$

$$A = \left(-\frac{B}{2}y, \frac{B}{2}x, 0\right).$$

The last is the *symmetric* or *Dingle* gauge. We choose the first one, which is the *Landau* gauge, and for which lines of constant A run in the x-direction. Then the Schrödinger equation in the real-space representation

$$\frac{1}{2m^*}\left[(p_x - eBy)^2 + p_y^2 + p_z^2\right]\psi + V(z)\psi = \mathcal{E}\psi$$

can be expressed using the canonical momentum operator $p \rightarrow -i\hbar\nabla$ as

$$\frac{1}{2m^*}\left[-\hbar^2\frac{\partial^2}{\partial x^2} + 2i\hbar eBy\frac{\partial}{\partial x} + (eBy)^2\right.$$
$$\left. - \hbar^2\frac{\partial^2}{\partial y^2} - \hbar^2\frac{\partial^2}{\partial z^2}\right]\psi + V(z)\psi = \mathcal{E}\psi. \qquad (A.2)$$

The form of the equation suggests a solution of the form $\psi = \exp(ikx)\phi(y)u(z)$. Substitution gives, after a little rearrangement

$$\left[-\frac{\hbar^2}{2m^*}\frac{\partial^2}{\partial y^2} + \frac{\hbar^2}{2m^*}k^2 - \frac{2\hbar eBy}{2m^*}k + \frac{(eBy)^2}{2m^*}\right]\phi(y)u(z)$$
$$+ \left[-\frac{\hbar^2}{2m^*}\frac{\partial^2}{\partial z^2} + V(z)\right]\phi(y)u(z) = \mathcal{E}\phi(y)u(z).$$

The x-, y- and z-motions thus separate. Writing the total energy $\mathcal{E} = \epsilon + \xi$ we have

$$\left(-\frac{\hbar^2}{2m^*}\frac{\partial^2}{\partial z^2} + V(z)\right)u(z) = \xi u(z) \qquad (A.3)$$

for the z-component. The eigensolutions $u_i(z)$, which of course depend on the particular confining potential $V(z)$, and the corresponding energy eigenvalues (or so-called 'subbands') ξ_i are labelled by the subband index i, which is normally taken as an integer running from 0 (the lowest energy subband) upwards. Similarly for the y-component

$$\left[-\frac{\hbar^2}{2m^*}\frac{\partial^2}{\partial y^2} - \hbar\omega_c ky + \frac{m^*\omega_c^2 y^2}{2} + \frac{\hbar^2}{2m^*}k^2\right]\phi(y) = \epsilon\phi(y)$$
$$(A.4)$$

where $\omega_c = eB/m^*$ is the cyclotron frequency. This can be written in the form of 1D simple harmonic motion in the y-direction

$$\left[-\frac{\hbar^2}{2m^*}\frac{\partial^2}{\partial y^2} + \frac{m^*\omega_c^2}{2}\left(y - \frac{\hbar k}{m^*\omega_c}\right)^2\right]\phi(y) = \epsilon\phi(y) \quad (A.5)$$

where we can write

$$y_k = \frac{\hbar k}{m^*\omega_c} = \frac{\hbar}{eB}k = l_B^2 k \qquad (A.6)$$

which is the centre of motion. The solutions for ϵ are simply

$$\epsilon_\ell = \hbar\omega_c\left(\ell + \tfrac{1}{2}\right) \qquad \text{where } \ell = 0, 1, 2\ldots. \qquad (A.7)$$

This is independent of the subband index, and the physical interpretation is that the applied magnetic field imposes additional quantization (Landau quantization) on the energy of each subband. In the cases of interest in this review, the subband energy separations are normally much larger than the Landau-level separations $\hbar\omega_c$. Additionally, the electron density is low enough to give occupancy of only the lowest subband (or lowest few subbands).

The term y_k is often expressed, as above, in terms of the *magnetic length*

$$l_B = (\hbar/m^*\omega_c)^{1/2} = (\hbar/eB)^{1/2}. \qquad (A.8)$$

Landau-level degeneracy; no spin

The in-plane part of the wavefunction is $\exp(ikx)\phi(y)$ with energy given by (A.7). The ℓ-states are highly degenerate as they are independent of the value of y_k. Taking periodic boundary conditions with length L_x in the x-direction allows us to count the states:

$$k = \frac{2\pi}{L_x}n_x, \qquad n_x = 0, \pm 1, \pm 2, \ldots$$

and the centres of the simple harmonic motion take the possible values $y_k = (2\pi l_B^2/L_x)n_x$. The centre of the wavefunction in the y-direction we take to be constrained between 0 and L_y and the number of allowed y_k values is thus $L_y/\Delta y_k = L_x L_y/2\pi l_B^2 = L_x L_y \times eB/h$ for each value of n. The degeneracy *per unit area* of the sample is thus, if we multiply by a factor two to include spin degeneracy,

$$g_L = 2eB/h. \qquad (A.9)$$

Wavefunctions

The in-plane part of the wavefunction takes the form of plane waves $\exp(ikx)$ in the x-direction and simple harmonic oscillator wavefunctions (the solutions of (A.5)) in the y-direction:

$$\phi(y) \propto H_\ell\left(\frac{y - y_k}{l_B}\right)\exp\left[-\frac{1}{2}\left(\frac{y - y_k}{l_B}\right)^2\right],$$

where H_ℓ are Hermite polynomials. The wavefunctions $\exp(ikx)\phi(y)$ are thus parallel strips in the x-direction (along the lines of constant A), with equal spacing along the y-direction given by $\Delta y_k/l_B = 2\pi l_B/L_x$. Since $l_B \sim 26$ nm at a field of ~ 1 T, the wavefunctions overlap each other very significantly in real space. The group velocity of the $|\ell, k\rangle$ state is

$$v(\ell, k) = \frac{1}{\hbar}\left(\frac{\partial\epsilon_\ell}{\partial k}\right) = 0$$

so these states carry no electric current. Although the states are extended in the x-direction and confined in the y-direction, because of the massive degeneracy, linear combinations of the $|\ell, k\rangle$ states exist which are confined in both directions and so are localized. Application of electric fields and/or impurity potentials will lift the degeneracy however, and remove the freedom to choose between localized and extended states.

Appendix B. Free electron in 2D in crossed fields

If we now add a uniform electric field $E = (0, E, 0)$ in the y-direction, the Schrödinger equation (A.2) gains an additional term $eEy\psi$ added to the left-hand side. The same separation of variables can be made as before and (A.5) becomes

$$\left[-\frac{\hbar^2}{2m^*}\frac{\partial^2}{\partial y^2} + \frac{m^*\omega_c^2}{2}\left(y - \frac{\hbar k}{m^*\omega_c}\right)^2 + eEy\right]\phi(y)$$
$$= \epsilon\phi(y). \tag{B.1}$$

This can still be written in the form of 1D simple harmonic motion in the y-direction

$$\left[-\frac{\hbar^2}{2m^*}\frac{\partial^2}{\partial y^2} + \frac{m^*\omega_c^2}{2}(y - y_k)^2 + \frac{\hbar k E}{B} - \frac{m^* E^2}{2B^2}\right]\phi(y)$$
$$= \epsilon\phi(y) \tag{B.2}$$

where the new centre of motion is

$$y_k = \frac{\hbar k}{m^*\omega_c} - \frac{eE}{m^*\omega_c^2} = \frac{\hbar k - m^* v_d}{eB}, \tag{B.3}$$

using $v_d = E/B$ the classical drift velocity. The solutions of (B.2) are, by comparison with (A.5) and (A.7)

$$\epsilon_l = \hbar\omega_c\left(\ell + \tfrac{1}{2}\right) + eEy_k + \tfrac{1}{2}m^* v_d^2. \tag{B.4}$$

The physical interpretation of this equation is that the LL energies expressed by (A.7) in zero applied electric field are shifted by an electrostatic potential energy term eEy_k and a kinetic energy term $\frac{1}{2}m^* v_d^2$. From the last two equations the group velocity is now

$$v(\ell, k) = \frac{1}{\hbar}\left(\frac{\partial \epsilon_\ell}{\partial k}\right) = E/B. \tag{B.5}$$

Appendix C. Model of capacitance in induced eddy currents

In the QH regime, any circulating eddy currents must be associated with a nearly perpendicular (Hall) electric field. We consider here a model (figure 12) in which the current density j_x at some position flows concentrated in a region of effective width w (the distance over which the Hall field is mostly dropped), supported by the Hall field E_y. (For example, current may flow parallel to the sample edge, concentrated near to the sample edge—but our model extends to a more general case.) The charge/discharge current density j_y across this region is written

$$j_y = -Cw\dot{E}_y \tag{C.1}$$

where C is the capacitance per unit length of the region. From Ohm's law we have

$$\begin{pmatrix} j_x \\ j_y \end{pmatrix} = \begin{pmatrix} \sigma_{xx} & \sigma_{xy} \\ -\sigma_{xy} & \sigma_{xx} \end{pmatrix} \begin{pmatrix} E_x \\ E_y \end{pmatrix}. \tag{C.2}$$

Discharge

First consider the case where the magnetic field has been swept to an eddy current peak and then stopped. Then $E_x = 0$ and the region has an initial charge on either side. Substituting (C.1) and $E_x = 0$ in Ohm's law gives

$$j_x = \sigma_{xy}E_y \qquad j_y = -Cw\dot{E}_y = \sigma_{xx}E_y. \tag{C.3}$$

The equation for E_y has solution

$$E_y = E_y(0)\exp(-t/\tau) \tag{C.4}$$

where the decay time constant is

$$\tau = Cw/\sigma_{xx} \tag{C.5}$$

and from (C.3)

$$j_x = j_x(0)\exp(-t/\tau). \tag{C.6}$$

Charge up

Capacitance should also be important in the case that the magnetic field is swept to an eddy current peak, starting with zero charge. Assuming a current flowing near the sample edge, then $E_x = \epsilon$ say, with ϵ related to the sample radius R and the sweep rate $\dot{B}$ approximately as

$$\epsilon \approx -\frac{R}{2}\dot{B}. \tag{C.7}$$

Instead of (C.3) we get, substituting (C.1) and $E_x = \epsilon$ in Ohm's law

$$j_x = \sigma_{xx}\epsilon + \sigma_{xy}E_y$$
$$j_y = -Cw\dot{E}_y = -\sigma_{xy}\epsilon + \sigma_{xx}E_y. \tag{C.8}$$

The equation for E_y has solution

$$E_y = \frac{\sigma_{xy}}{\sigma_{xx}}\epsilon(1 - \exp(-t/\tau)) \tag{C.9}$$

where the time constant is as before

$$\tau = Cw/\sigma_{xx} \tag{C.10}$$

and from (C.8)

$$j_x \approx \frac{\sigma_{xy}^2}{\sigma_{xx}}\epsilon(1 - \exp(-t/\tau)). \tag{C.11}$$

The main approximation in this charge-up picture is neglecting the time dependence of σ_{xx} during the field sweep in integrating (C.8). In particular, from (C.9), if σ_{xx} is sufficiently small, or ϵ is sufficiently large, E_y might reach breakdown. This would have the effect of increasing σ_{xx} to give a much faster charge-up time τ. The model furthermore needs an estimate of w in order to calculate actual current densities, and hence E_y, from experimental values of magnetic moment.

A rough estimate of the *maximum* peak height as a function of sweep rate can be obtained by assuming that σ_{xx} is small (and constant) over a field width ΔB. The time Δt

28

to sweep to the centre of the peak is $\Delta B/2\dot{B}$, and substituting into (C.11) gives

$$j_x^{\text{peak}} \approx \frac{\sigma_{xy}^2}{\sigma_{xx}} \epsilon \left(1 - \exp\left(-\Delta B/2\dot{B}\tau\right)\right). \qquad \text{(C.12)}$$

It is interesting to examine the dissipation $\boldsymbol{j} \cdot \boldsymbol{E}$ during the charge-up process. Because we are not dealing with a Hall bar, an *increase* in σ_{xx} can actually lead to a *decrease* in dissipation. This follows from (C.8)

$$\boldsymbol{j} \cdot \boldsymbol{E} = \left(j_x E_x + j_y E_y\right) = \sigma_{xx}\left(\epsilon^2 + E_y^2\right). \qquad \text{(C.13)}$$

Just before breakdown, the Hall field E_y is much larger than the imposed field ϵ, and the sudden decrease in E_y as breakdown begins causes a decrease in dissipation. An analysis based on (C.9), gives $\boldsymbol{j} \cdot \boldsymbol{E} = \sigma_{xx}\epsilon^2$ when $t = 0$, i.e. before the Hall field has been established, $\boldsymbol{j} \cdot \boldsymbol{E} \sim \sigma_{xx}\epsilon^2(t\sigma_{xx}/Cw)$ when the field is starting to build ($t \ll \tau$) and

$$\boldsymbol{j} \cdot \boldsymbol{E} \sim \sigma_{xx}\epsilon^2 \left(1 + \left(\sigma_{xy}/\sigma_{xx}\right)^2\right) \sim \epsilon^2 \left(\sigma_{xy}^2\right)/\sigma_{xx} \qquad \text{(C.14)}$$

once the Hall field is well established. This last equation shows that an increase in σ_{xx} produces a decrease in dissipation, so that breakdown is self-limiting.

References

[1] Störmer H L, Haavasoja T, Narayanamurti V, Gossard A C and Wiegmann W 1983 *J. Vac. Sci. Technol.* B **1** 423–6
[2] Meinel I, Grundler D, Bargstädt-Franke S, Heyn C, Heitmann D and David B 1997 *Appl. Phys. Lett.* **70** 3305–7
[3] Meinel I, Hengstmann T, Grundler D, Heitmann D, Wegscheider W and Bichler M 1999 *Phys. Rev. Lett.* **82** 819–22
[4] Faulhaber D R and Jiang H W 2005 *Phys. Rev. B* **72** 233308
[5] de Haas W J and van Alphen P M 1930 *Proc. Neth. R. Acad. Sci.* **33** 1106
[6] Eisenstein J P 1985 *Appl. Phys. Lett.* **46** 695–6
[7] Haavasoja T, Störmer H L, Bishop D J, Narayanamurti V, Gossard A C and Wiegmann W 1984 *Surf. Sci.* **142** 294–7
[8] Eisenstein J P, Störmer H L, Narayanamurti V and Gossard A C 1985 *Superlatt. Microstruct.* **1** 11–4
[9] Eisenstein J P, Störmer H L, Narayanamurti V, Cho A Y, Gossard A C and Tu C W 1985 *Phys. Rev. Lett.* **55** 875–8
[10] Templeton I M 1988 *J. Appl. Phys.* **64** 3570–3
[11] Wiegers S A J, van Steenbergen A S, Jeuken M E, Bravin M, Wolf P E, Remenyi G, Perenboom J A A J and Maan J C 1998 *Rev. Sci. Instrum.* **69** 2369–74
[12] Matthews A J, Usher A and Williams C D H 2004 *Rev. Sci. Instrum.* **75** 2672–7
[13] Schaapman M R, Christianen P C M, Maan J C, Reuter D and Wieck A D 2002 *Appl. Phys. Lett.* **81** 1041–3
[14] Schwarz M P, Grundler D, Meinel I, Heyn C and Heitmann D 2000 *Appl. Phys. Lett.* **76** 3564–6
[15] Hayne M, Usher A, Harris J J, Moshchalkov V V and Foxon C T 1998 *Phys. Rev. B* **57** 14813–7
[16] Crowell P A, Madouri A, Specht M, Chaboussant G, Mailly D and Levy L P 1996 *Rev. Sci. Instrum.* **67** 4161–6
[17] Springborn J I, Ruhe N, Heyn C, Wilde M A, Heitmann D and Grundler D 2006 *Physica* E **34** 172–5
[18] Ruhe N, Springborn J I, Heyn C, Wilde M A and Grundler D 2006 *Phys. Rev. B* **74** 235326
[19] Harris J G E, Awschalom D D, Maranowski K D and Gossard A C 2000 *J. Appl. Phys.* **87** 5102–4
[20] de Haas W J and van Alphen P M 1930 *Comm. Phys. Lab. Leiden* 208d, 212a
[21] Landau L 1930 *Z. Phys.* A **64** 629–37
[22] Peierls R E 1933 *Z. Phys.* A **81** 186–94
[23] Peierls R E and Dalitz R H 1996 *Selected Scientific Papers of Sir Rudolf Peierls: With Commentary* (Singapore: World Scientific) ISBN 9810226934
[24] Shoenberg D 1984 *Magnetic Oscillations in Metals* (Cambridge: Cambridge University Press)
[25] Lifshitz I M and Kosevich A M 1954 *Dokl. Akad. Nauk SSSR* **96** 963
[26] Lifshitz I M and Kosevich A M 1956 *Sov. Phys.—JETP* **2** 636–45
[27] Dingle R B 1952 *Proc. R. Soc.* A **211** 517–25
[28] Brailsford A D 1966 *Phys. Rev.* **149** 456–63
[29] Středa P 1974 *Czech. J. Phys.* B **24** 794
[30] Luttinger J M 1961 *Phys. Rev.* **121** 1251–8
[31] Engelsberg S and Simpson G 1970 *Phys. Rev. B* **2** 1657–65
[32] Wasserman A and Springford M 1996 *Adv. Phys.* **45** 471–503
[33] Kishigi K and Hasegawa Y 2005 *Phys. Rev. B* **72** 045410
[34] Dresselhaus M S and Dresselhaus G 2002 *Adv. Phys.* **51** 1–186
[35] Neto A H C, Guinea F, Peres N M R, Novoselov K S and Geim A K 2007 arXiv:0709.1163v2
[36] Singleton J 2000 *Rep. Prog. Phys.* **63** 1111–207
[37] Champel T 2001 *Phys. Rev. B* **64** 054407
[38] Champel T and Mineev V P 2001 *Phil. Mag. B* **81** 55–74
[39] Kishigi K and Hasegawa Y 2002 *Phys. Rev. B* **65** 205405
[40] Curnoe S and Stamp P C E 1998 *Phys. Rev. Lett.* **80** 3312–5
[41] Martin G W, Maslov D L and Reizer M Y 2003 *Phys. Rev. B* **68** 241309
[42] Ando T and Murayama Y 1985 *J. Phys. Soc. Japan* **54** 1519–27
[43] Cai W and Ting C S 1986 *Phys. Rev. B* **33** 3967–72
[44] Esfarjani K, Glyde H R and Sa-yakanit V 1990 *Phys. Rev. B* **41** 1042–53
[45] Wang J K, Campbell J H, Tsui D C and Cho A Y 1988 *Phys. Rev. B* **38** 6174–84
[46] Heitman D, Ziesmann M and Chang L L 1986 *Phys. Rev. B* **34** 7463–6
[47] Smith T P, Goldberg B B, Stiles P J and Heiblum M 1985 *Phys. Rev. B* **32** 2696–9
[48] Smith T P, Wang W I and Stiles P J 1986 *Phys. Rev. B* **34** 2995–8
[49] Zheng H, Song A, Yang F and Li Y 1994 *Phys. Rev. B* **49** 1802–8
[50] Ashoori R C and Silsbee R H 1992 *Solid State Commun.* **81** 821–5
[51] Potts A, Shepherd R, Herrenden-Harker W G, Elliott M, Jones C L, Usher A, Jones G A C, Ritchie D A, Linfield E H and Grimshaw M 1996 *J. Phys.: Condens. Matter* **8** 5189–207
[52] Glutsch S, Bechstedt F and Quang D N 2003 *J. Phys.: Condens. Matter* **15** 1305–23
[53] Elliott M 1998 Notes on the dHvA effect in 2DEG, unpublished
[54] Betts D S and Turner R E 1992 *Introductory Statistical Mechanics* (Reading, MA: Addison-Wesley) chapter 11
[55] Zawadzki W 1983 *Solid State Commun.* **77** 317–20
[56] Harrison N, Bogaerts R, Reinders P H P, Singleton J, Blundell S J and Herlach F 1996 *Phys. Rev. B* **54** 9977–87
[57] Palin C J 1972 *Proc. R. Soc.* A **329** 17–34
[58] Elliott M, Ellis T and Springford M 1978 *Phys. Rev. Lett.* **41** 709–11
[59] Adamov Y, Gornyi I V and Mirlin A D 2006 *Phys. Rev. B* **73** 045426
[60] Pudalov V M, Gershenson M E, Kojima H, Butch N, Dizhur E M, Brunthaler G, Prinz A and Bauer G 2002 *Phys. Rev. Lett.* **88** 196404

[61] Shashkin A A, Rahimi M, Anissimova S, Kravchenko S V, Dolgopolov V T and Klapwijk T M 2003 *Phys. Rev. Lett.* **91** 046403

[62] Tan Y-W, Zhu J, Stormer H L, Pfeiffer L N, Baldwin K W and West K W 2005 *Phys. Rev. Lett.* **94** 016405

[63] Peierls R 1979 *Surprises in Theoretical Physics* (Princeton, NJ: Princeton University Press)

[64] Lorrain P, Corson D and Lorrain F 1987 *Electromagnetic Fields and Waves* 3rd edn (San Fransisco, CA: Freeman)

[65] Středa P and Smrčka L 1983 *J. Phys. C: Solid State Phys.* **16** L895–9

[66] Bremme L, Ihn T and Ensslin K 1999 *Phys. Rev.* B **59** 7305–7

[67] Halperin B I 1982 *Phys. Rev.* B **25** 2185–90

[68] Fang F F and Stiles P J 1983 *Phys. Rev.* B **28** 6992–5

[69] Eisenstein J P, Störmer H L, Narayanamurti V, Cho A Y and Gossard A C 1985 *Surf. Sci.* **170** 271–6

[70] Elliott M, Harris M G M, Herrenden-Harker W G, Shepherd R, Jones G A C, Ritchie D A, Linfield E H and Grimshaw M 1994 *ICFSI-4 Proc. 4th Int. Conf. on the Formation of Semiconductors Interfaces (Julich, June 1993)* (Singapore: World Scientific) chapter VI, p 64 14 ISBN 981-02-1559-2

[71] Zhu M, Usher A, Matthews A J, Potts A, Elliott M, Herrenden-Harker W G, Ritchie D A and Simmons M Y 2003 *Phys. Rev.* B **67** 155329

[72] Usher A, Zhu M, Matthews A J, Potts A, Elliott M, Herrenden-Harker W G, Ritchie D A and Simmons M Y 2004 *Physica* E **22** 741–4

[73] Wiegers S A J, Specht M, Lévy L P, Simmons M Y, Ritchie D A, Cavanna A, Etienne B, Martinez G and Wyder P 1997 *Phys. Rev. Lett.* **79** 3238–41

[74] Schwarz M P, Grundler D, Rolff H, Wilde M, Groth S, Heyn C and Heitmann D 2002 *Physica* E **12** 140–3

[75] Schwarz M P, Wilde M A, Groth S, Grundler D, Heyn C and Heitmann D 2002 *Phys. Rev.* B **65** 245315

[76] Gornik E, Lassnig R, Strasser G, Störmer H L, Gossard A C and Wiegmann W 1985 *Phys. Rev. Lett.* **54** 1820–3

[77] Wilde M A, Springborn J I, Roesler O, Ruhe N, Schwarz M P, Heitmann D and Grundler D 2008 *Phys. Status Solidi* **245** 344–55

[78] Xu W 1994 *Phys. Rev.* B **50** 14601–4

[79] Raymond A, Juillaguet S, Elmezouar I, Zawadzki W, Sadowski M L, Kamal-Saadi M and Etienne B 1999 *Semicond. Sci. Technol.* **14** 915–20

[80] Shepherd R A, Elliott M, Herrenden-Harker W G, Zervos M, Morris P R, Beck M and Ilegems M 1999 *Phys. Rev.* B **60** R11277–80

[81] Singleton J, Harrison N, Bogaerts R, Reinders P H P, Deckers I, Blundell S J and Herlach F 1997 *Synth. Met.* **86** 1907–8

[82] Coleridge P T 1990 *Semicond. Sci. Technol.* **5** 961–6

[83] Watts B R 1986 *J. Phys. F: Met. Phys.* **16** 141–6

[84] Watts B R 1986 *J. Phys. F: Met. Phys.* **16** 147–56

[85] Singleton J, McDonald R and Harrison N 2008 *The Physics of Organic Superconductors and Conductors* (*Springer Series in Materials Science* vol 110) ed A G Lebed (Berlin: Springer) pp 247–76

[86] Watts B R 1977 *J. Phys. F: Met. Phys.* **7** 929–37

[87] Watts B R 1974 *J. Phys. F: Met. Phys.* **4** 1387–91

[88] Watts B R 1974 *J. Phys. F: Met. Phys.* **4** 1371–86

[89] Harrison N and Singleton J 2001 *J. Phys.: Condens. Matter* **13** L463–7

[90] Woltjer R, Eppenga R, Mooren J, Timmering C E and André J P 1986 *Europhys. Lett.* **2** 149–55

[91] Woltjer R 1988 *Surf. Sci.* **196** 188–95

[92] Woltjer R 1989 *Semicond. Sci. Technol.* **4** 155–67

[93] Gudmundsson V and Gerhardts R R 1987 *Phys. Rev.* B **35** 8005–14

[94] Raymond A and Sibari H 1994 *Phys. Status Solidi* **183** 159–73

[95] Kerridge G C, Greally M G, Hayne M, Usher A, Plaut A S, Brum J A, Holland M C and Stanley C R 1999 *Solid State Commun.* **109** 267

[96] Manasreh M O, Fischer D W, Evans K R and Stutz C E 1991 *Phys. Rev.* B **43** 9772–6

[97] Schaapman M R, Zeitler U, Christianen P C M, Maan J C, Reuter D, Wieck A D, Schuh D and Bichler M 2003 *Phys. Rev.* B **68** 193308

[98] Zawadzki W, Bonifacie S, Juillaguet S, Chaubet C, Raymond A, Meziani Y M, Kubisa M and Ryczko K 2007 *Phys. Rev.* B **75** 245319

[99] Toyoda T, Hiraiwa N, Fukuda T and Koizumi H 2008 *Phys. Rev. Lett.* **100** 036802

[100] Alexandrov A S and Bratkovsky A M 1996 *Phys. Rev. Lett.* **76** 1308–11

[101] Alexandrov A S and Bratkovsky A M 1997 *Phys. Lett.* A **234** 53–8

[102] Alexandrov A S and Bratkovsky A M 2001 *Phys. Rev.* B **63** 033105

[103] Portal J C, Nicholas R J, Brummell M A, Cho A Y, Cheng K Y and Pearsall T P 1982 *Solid State Commun.* **43** 907–11 ISSN 0038-1098

[104] Champel T 2002 *Phys. Rev.* B **65** 153403

[105] Alexandrov A S and Bratkovsky A M 2004 *Phys. Rev.* B **69** 167401

[106] Champel T 2004 *Phys. Rev.* B **69** 167402

[107] Chakraborty T and Pietiläinen P 1995 *The Quantum Hall Effects: Integral and Fractional* (*Springer Series in Solid-State Sciences* vol 85) (Berlin: Springer)

[108] Macdonald A H, Oji H C A and Liu K L 1986 *Phys. Rev.* B **34** 2681–9

[109] Fock V 1928 *Z. Phys.* **47** 446–8

[110] Darwin C G 1931 *Proc. Camb. Phil. Soc.* **27** 86–90

[111] Meir Y, Entinwohlman O and Gefen Y 1990 *Phys. Rev.* B **42** 8351–60

[112] Fogler M M, Levin E I and Shklovskii B I 1994 *Phys. Rev.* B **49** 13767–75

[113] Wilde M A, Springborn J I, Heyn C, Heitmann D and Grundler D 2004 *Physica* E **22** 729–32

[114] Alexandrov A S and Kabanov V V 2005 *Phys. Rev. Lett.* **95** 076601

[115] von Klitzing K, Dorda G and Pepper M 1980 *Phys. Rev. Lett.* **45** 494–7

[116] Klass U, Dietsche W, von Klitzing K and Ploog K 1991 *Physica* B **169** 363–7

[117] Kent A J, Mckitterick D J, Challis L J, Hawker P, Mellor C J and Henini M 1992 *Phys. Rev. Lett.* **69** 1684–6

[118] Komiyama S, Kawaguchi Y, Osada T and Shiraki Y 1996 *Phys. Rev. Lett.* **77** 558–61

[119] Komiyama S and Kawaguchi Y 2000 *Phys. Rev.* B **61** 2014–27

[120] Macdonald A H, Rice T M and Brinkman W F 1983 *Phys. Rev.* B **28** 3648–50

[121] Morris P R, Elliott M, Herrenden-Harker W G, Usher A, Watts J P, Matthews A J, Sorensen C B and Hansen O P 1999 *Proc. 24th ICPS 1998* (Singapore: World Scientific) ISBN 981-02-3613-1

[122] Jones C L, Usher A, Elliott M, Herrenden-Harker W G, Potts A, Shepherd R, Cheng T S and Foxon C T 1995 *Solid State Commun.* **95** 409–13

[123] Jones C L, Usher A, Elliott M, Herrenden-Harker W G, Potts A, Shepherd R, Cheng T S and Foxon C T 1996 *Solid State Commun.* **97** 763–8

[124] Watts J P, Usher A, Matthews A J, Zhu M, Elliott M, Herrenden-Harker W G, Morris P R, Simmons M Y and Ritchie D A 1998 *Phys. Rev. Lett.* **81** 4220–3

[125] Kershaw T J, Usher A, Sachrajda A S, Gupta J, Wasilewski Z R, Elliott M, Ritchie D A and Simmons M Y 2007 *New J. Phys.* **9** 71

[126] Klaffs T, Krupenin V A, Weis J and Ahlers F J 2004 *Physica* E **22** 737–40
[127] Huels J, Weis J, Smet J, von Klitzing K and Wasilewski Z R 2004 *Phys. Rev.* B **69** 085319
[128] Pioro-Ladrière M, Usher A, Sachrajda A S, Lapointe J, Gupta J, Wasilewski Z, Studenikin S and Elliott M 2006 *Phys. Rev.* B **73** 075309
[129] Pioro-Ladrière M, Usher A, Sachrajda A S, Elliott M, Lapointe J, Gupta J, Wasilewski Z R and Studenikin S 2006 *Physica* E **34** 476–9
[130] Nachtwei G 1999 *Physica* E **4** 79–101
[131] Ebert G, von Klitzing K, Ploog K and Weimann G 1983 *J. Phys. C: Solid State Phys.* **16** 5441–8
[132] Buttiker M 1988 *Phys. Rev.* B **38** 9375–89
[133] Beenakker C W J and van Houten H 1991 *Quantum Transport in Semiconductor Nanostructures* (*Solid State Physics* vol 44) (New York: Academic)
[134] Datta S 1995 *Electronic Transport in Mesoscopic Systems* (Cambridge: Cambridge University Press)
[135] Tsemekhman K, Tsemekhman V, Wexler C and Thouless D J 1997 *Solid State Commun.* **101** 549–53
[136] Chklovskii D B, Shklovskii B I and Glazman L I 1992 *Phys. Rev.* B **46** 4026–34
[137] Yacoby A, Fulton T A, Hess H F, Pfeiffer L N and West K W 2003 *Physica* E **20** 65–70
[138] Shizuya K 1994 *Phys. Rev. Lett.* **73** 2907–10
[139] Balaban N Q, Meirav U, Shtrikman H and Levinson Y 1993 *Phys. Rev. Lett.* **71** 1443–6
[140] Cage M E, Dziuba R F, Field B F, Williams E R, Girvin S M, Gossard A C, Tsui D C and Wagner R J 1983 *Phys. Rev. Lett.* **51** 1374–7
[141] Kuchar F, Bauer G, Weimann G and Burkhard H 1984 *Surf. Sci.* **142** 196–202
[142] Störmer H L, Chang A M, Tsui D C and Hwang J C M 1999 *Proc. 17th Int. Conf. on the Physics of Semiconductors (San Francisco, 1998)* (Berlin: Springer) ISBN 038-79-6108-9
[143] Kawaji S, Hirakawa K, Nagata M, Okamoto T, Fukase T and Gotoh T 1994 *J. Phys. Soc. Japan* **63** 2303–13
[144] Meirav U, Balaban N Q and Shtrikman H 1995 *High Magnetic Fields in the Physics of Semiconductors* (Singapore: World Scientific) ISBN 981-02-2181-9
[145] Komiyama S, Takamasu T, Hiyamizu S and Sasa S 1985 *Solid State Commun.* **54** 479–48
[146] Takamasu T, Komiyama S, Hiyamizu S and Sasa S 1986 *Surf. Sci.* **170** 202–8
[147] Středa P and von Klitzing K 1984 *J. Phys. C: Solid State Phys.* **17** L483–6
[148] Tsemekhman V, Tsemekhman K, Wexler C, Han J H and Thouless D J 1997 *Phys. Rev.* B **55** 10201–4
[149] Heinonen O, Taylor P L and Girvin S M 1984 *Phys. Rev.* B **30** 3016–9
[150] Eaves L, Guimaraes P S S, Portal J C, Pearsall T P and Hill G 1984 *Phys. Rev. Lett.* **53** 608–11
[151] Eaves L and Sheard F W 1986 *Semicond. Sci. Technol.* **1** 346–9
[152] Ahlers F J, Hein G, Scherer H, Bliek L, Nickel H, Losch R and Schlapp W 1993 *Semicond. Sci. Technol.* **8** 2062–8
[153] Bliek L, Braun E, Hein G, Kose V, Niemeyer J, Weimann G and Schlapp W 1986 *Semicond. Sci. Technol.* **1** 110–2

[154] Yokoi M *et al* 1998 *Physica* B **249–251** 93
[155] Jeanneter B *et al* 1995 *Phys. Rev.* B **51** 9752
[156] Hansen O P 1990 *Superlatt. Microstruct.* **8** 365
[157] Petersen P L 1995 *Master's Thesis* University of Copenhagen
[158] Laughlin R B 1981 *Phys. Rev.* B **23** 5632
[159] Matthews A J, Watts J P, Zhu M, Usher A, Elliott M, Herrenden-Harker W G, Morris P R, Simmons M Y and Ritchie D A 2000 *Physica* E **6** 140–3
[160] Jain J K 1989 *Phys. Rev. Lett.* **63** 199–202
[161] Leadley D R, Nicholas R J, Foxon C T and Harris J J 1994 *Phys. Rev. Lett.* **72** 1906–9
[162] Matthews A J, Kavokin K V, Usher A, Portnoi M E, Zhu M, Gething J D, Elliott M, Herrenden-Harker W G, Phillips K, Ritchie D A, Simmons M Y, Sorensen C B, Hansen O P, Mironov O A, Myronov M, Leadley D R and Henini M 2004 *Phys. Rev.* B **70** 075317
[163] Kavokin K V, Portnoi M E, Matthews A J, Usher A, Gething J, Ritchie D A and Simmons M Y 2005 *Solid State Commun.* **134** 257–9
[164] Gething J D, Matthews A J, Usher A, Portnoi M E, Kavokin K V and Henini M 2004 *Int. J. Mod. Phys.* B **18** 3537–40
[165] Gething J D, Matthews A J, Usher A, Portnoi M E, Kavokin K V and Henini M 2005 *Proc. 27th Int. Conf. on the Phys. of Semicond.* vol 772, ed J Menendez and C G Van de Walle pp 561–2
[166] Dyakonov M I 1991 *Solid State Commun.* **78** 817–21
[167] Gerhardts R R and Gudmundsson V 1986 *Phys. Rev.* B **34** 2999–3003
[168] Matthews A J, Kavokin K V, Usher A, Portnoi M E, Gething J D, Zhu M and Ritchie D A 2004 *Int. J. Mod. Phys.* B **18** 3593–6
[169] Phillips K L, Elliott M, Lu Y, Herrenden-Harker W G, Matthews A J, Gething J D, Usher A, Henini M, Ritchie D A and Simmons M Y 2004 *Physica* E **22** 210–3
[170] Elliott M, Lu Y, Phillips K L, Herrenden-Harker W G, Usher A, Matthews A J, Gething J, Zhu M, Henini M and Ritchie D A 2006 *Europhys. Lett.* **75** 287–93
[171] Cage M E, Reedtz G M, Yu D Y and Degrift C T V 1990 *Semicond. Sci. Technol.* **5** 351–4
[172] Song A M and Omling P 2000 *Phys. Rev. Lett.* **84** 3145–8
[173] Boella G, Cordiali L, Marullo-Reedtz G, Allasia D, Rinaudo G, Truccato M and Villavecchia C 1994 *Phys. Rev.* B **50** 7608–14
[174] Bak P, Tang C and Wiesenfeld K 1988 *Phys. Rev.* A **38** 364–74
[175] Chapman S C 1998 *Physics of Space Plasmas* (Cambridge, MA: MIT Center for Theoretical Geo/Cosmo Plasma Physics) p 67
[176] Dendy R O and Helander P 1998 *Phys. Rev.* E **57** 3641–4
[177] Christensen K 2005 private communication
[178] Tsemekhman K, Tsemekhman V and Wexler C 1998 arXiv:cond-mat/9810076
[179] Tsemekhman K, Tsemekhman V and Wexler C 1998 arXiv:cond-mat/9812111v2
[180] Lo C F 1992 *Eur. J. Phys.* **13** 125–6
[181] Douçot B and Pasquier V 2005 *The Quantum Hall Effect: Poincaré Seminar 2004* (*Progress in Mathematical Physics* vol 45) (Basle: Birkhäuser,) pp 23–54